# Correlative cryogenic montage electron tomography for comprehensive in-situ whole-cell structural studies

Jie E. Yang[1,2,3], Matthew R. Larson[1,2,3,#], Bryan S. Sibert[1,2,3,#], Joseph Y. Kim[1,4,#], Daniel Parrell[1], Juan C. Sanchez[1,5], Victoria Pappas[1,5], Anil Kumar[1,2,3], Kai Cai[1,2,3], Keith Thompson[1,2,3], Elizabeth R. Wright[1,2,3,6,*]

[1]Department of Biochemistry, University of Wisconsin, Madison, WI USA

[2]Cryo-Electron Microscopy Research Center, Department of Biochemistry, University of Wisconsin, Madison, WI USA

[3]Midwest Center for Cryo-Electron Tomography, Department of Biochemistry, University of Wisconsin, Madison, WI USA

[4]Department of Chemistry, University of Wisconsin, Madison, WI USA

[5]Biophysics Graduate Program, University of Wisconsin, Madison, WI USA

[6]Morgridge Institute for Research, Madison, WI, USA

[#]These authors contributed equally

*To whom correspondence should be addressed.

E-mail: erwright2@wisc.edu; Tel.: (+1) 608-265-0666; Fax: (+1) 608-265-4693

## Abstract

**Imaging large fields of view while preserving high-resolution structural information remains a challenge in low-dose cryo-electron tomography. Here, we present robust tools for montage electron tomography tailored for vitrified specimens. The integration of correlative cryo-fluorescence microscopy, focused-ion beam milling, and micropatterning produces contextual three-dimensional architecture of cells. Montage tilt series may be processed in their entirety or as individual tiles suitable for sub-tomogram averaging, enabling efficient data processing and analysis.**

## Main

There is an increasing interest and need for a comprehensive understanding of the structure and function of macromolecules, both isolated and within the context of a larger biological system. While cryo-electron microscopy (cryo-EM) of purified proteins (e.g., single-particle cryo-EM) has propelled the cryo-EM 'resolution resolution'[1], *ex-situ* conditions may not capture cellular interactions taking place between biological molecules in a native context. Cryo-electron tomography (cryo-ET) links three-dimensional (3D) contextual visualization and high-resolution structure determination of cryogenically preserved macromolecular complexes in their native cellular environment[2], unperturbed by purification or chemical fixation and staining[3,4]. Computationally extracted sub-tomograms can be analyzed and classified to reveal sub-nanometer (sub-5 Å) to nanometer (1~3 nm) resolution structures of *in-situ* complexes[5]. Cryo-ET is generally restricted to investigations of small specimen volumes and the thin peripheral areas of cells (< 500 nm) that are penetrable by the electron beam. To explore thicker regions of

cells, sample thinning technologies have evolved and include cryo-electron microscopy of vitreous sections (CEMOVIS)[6] and cryo-focused ion beam (cryo-FIB) milling[7]. Both methods produce thin sections or lamella from bulk materials, but each may be impacted by preparative artifacts such as sample compression or curtaining, respectively. Cryo-correlative light and electron microscopy (cryo-CLEM)[8] correlates the temporal and spatial information from fluorescence light microscopy (FLM), with ultrastructural data from cryo-ET of the same region of interest (ROI) while retaining context. In combination with cryo-FIB milling, it is now possible to pinpoint an area of interest deep in the interior of a specimen through 3D correlative cryo-FLM-FIB-ET[9]. However, it remains challenging to bridge the disparity of the spatial scales in multi-modal microscopy pipelines where the field of view (FOV) in wide-field FLM can be $10^5$ times (~0.1 to 5 mm) that of an EM FOV (~200 nm to 800 μm)[2,10].

In cryo-ET, tilt series acquisition of an ROI involves tilting the cryo-preserved specimen along one or two axes[11] while a series of projection images is incrementally captured on a detector. Tilt series of the same region could be collected at both high and low magnifications for subsequent reconstruction into 3D tomograms to obtain high-resolution structural information[12] and overall landscape visualization, respectively. However, this could be difficult to implement due to the radiation sensitivity of frozen-hydrated biological materials and the need to use low-dose exposure routines (~1-3 $e^-/Å^2$/tilt) that must maintain sufficient signal over background noise at each tilted image to support individual frame, image, and tilt series alignment. Advances in detector design have supported the use of larger format detectors for certain applications[13]. Of note, detector size scales

exponentially with the volume of the data being digitized, thus imposing challenges to hardware and software infrastructure[14]. These technical hurdles and others[5] have constrained the application of cryo-ET to fractional volumes of cells that result in significant losses to the FOV and contextual information. An approach for obtaining 3D tomograms that encompass a larger FOV is to collect montages of tilt series. The development of montage cryo-ET has been limited. To our knowledge, only one method[15] has been reported. As noted by the authors, major challenges included seamlessly joining cryo-EM montage tiles with improved automation[15], processing large volume stitched tomograms[16], and sub-tomogram averaging (STA).

Here, we demonstrate our adaptation of the principles of montage tomography, which is routinely applied to resin-embedded samples[17,18], to frozen-hydrated specimens via montage cryo-ET. This montage cryo-ET data collection routine and automated processing schemes (Supplementary Fig. 1) are robust solutions for the generation of molecular-level resolution 3D reconstructions of vitrified specimens.

We employed image-shift montage acquisition[17,19] to acquire overlapping tiles of defined size at each tilt increment. Rectangular or square montage tile patterns and tile overlaps were investigated while considering: 1) Fresnel fringes formed inside the image detector FOV from the C2 aperture of an electron microscope[20] introduce non-uniform illumination and disruption in image signals (Supplementary Fig. 2a). Under a magnification (4.6 Å/pixel) and defocus value (-5 $\mu m$) typical for cryo-ET collection, the beam fringe artifact was determined to affect up to 3 to 4% of the FOV extending from the

outer edge of the 3.11 $\mu m$ illuminated area (Supplementary Fig. 2b) when the outer edge of the beam intersected the camera at ~4% of its long axis. 2) Under parallel illumination, the beam size relative to the camera frame determines the captured FOV and fringe-unimpacted or 'fringeless' area (Supplementary Fig. 2c-d). The FOV affected by Fresnel fringes becomes increasingly evident as the beam size decreases under a constant magnification and defocus (Supplementary Fig. 2d-e). Yet, use of an expanded beam and larger illuminated areas to minimizing in-frame fringes also impacts the sample through excess pre-exposure irradiation (Supplementary Fig. 2c). 3) Robust automation of montage stitching at each tilt requires consistent overlap regions between adjacent tiles. Compared to resin-embedded samples where the image contrast is strong[18], reliable tile overlaps at a majority of the tilts are essential in vitrified unstained samples to achieve gap-free stitching[15]. 4) Sorting of individual tile tilt series from the complete montage collection for efficient data processing and sub-tomogram averaging is applicable only when each tile frame contains enough fringe-unimpacted FOV and retains the ROI throughout the tilt series.

An inherent limitation of montage cryo-ET is the uneven accumulation of dose in overlapping regions between adjacent tiles, which leads to excessive radiation damage. Therefore, we adopted an additional globally applied translation shift that was calculated from the central tile of a montage pattern (Supplementary Figs. 3, 4, 9a). To quantitatively assess cryo-ET data collection and montage tiling strategies, we developed TomoGrapher, a user-friendly simulation tool to visualize tilt series collection routines and determine global and localized electron dose accumulation (Supplementary Fig. 3).

TomoGrapher supports simulation of tilt series acquisition with and without a translational shift extending along spiral paths (Supplementary Fig. 4a-f, Table 1). The shape of the spiral trajectory can be adjusted to vary dose accumulation on each voxel over the full tilt range. Circular beam projections and the associated images gradually elongate to ellipses along the X-axis perpendicular to the tilt axis (Y-axis) as the tilt angle increases (Supplementary Figs. 3b, 4c-d), resulting in stretching of the spiral paths. Optional X-axial correction and cosine-weighting[21] of dose can be implemented in the simulation process (Supplementary Fig. 3). Within the maximum offset distance permitted to retain the FOV in the full tilt range, simulation results suggest larger translations and axial correction introduce more uniformly spread dose (Supplementary Fig. 4g-h).

Overall, both simulation results and experimental data demonstrate the incorporation of a global translational shift allowed for a more even distribution of the total electron dose across each montage tile and tile overlap regions where accumulated dose would otherwise be much higher (Supplementary Fig. 4, Table 1). We determined that a 15 to 20% overlap in X (fringe-affected axis) and 10% in Y (fringe-unaffected axis) of tile frames was sufficient for automated gap-free tile stitching without human intervention at tilt angles up to $\pm$39° and minimal manual fixation at higher tilt angles ($\pm$ 40° to 60°) using coordinate-based image cross-correlation[22] (Supplementary Figs. 5a-c). We explored the addition of rotation to translation of the tile montage pattern to further spread the dose. Our data (Supplementary Fig. 5d) support a common observation that rotation of the in-plane image shift deviates significantly from the designated coordinates as the stage tilt increases[23]. This departure in image shift values introduced by global tile rotation was

much larger than the applied translation alone at lower tilts and became particularly irregular as the stage was tilted to degrees greater than ±30°. As a result, the inconsistent overlap between tiles caused problematic stitching, consistent with previous reports[15,18].

We integrated montage cryo-ET with 2D and 3D correlative cryo-CLEM and cryo-FIB routines using CorRelator[24], 3DCT[9], and SerialEM[19] to image large, targeted FOV along the periphery of HeLa cells (Supplementary Fig. 6) and cryo-FIB-milled lamella near the nucleus of adenocarcinomic human alveolar basal epithelial (A549) cells (Fig. 1, Supplementary Fig. 7). Both cell lines are commonly used for studies of both mitochondrial function and respiratory syncytial virus (RSV) infection[25,26]. A pixel size of 4.6 Å was used to support the large FOV and STA sampling requirements[12]. 2D cryo-CLEM was applied to identify fields of long, filamentous RSV particles budding from metabolically active RSV-infected HeLa cells[26] for montage cryo-ET data collection (Supplementary Fig. 6). Montage tomograms of RSV particles up to 8 $\mu m$ in length revealed the ultrastructure of intact virions and organization of viral compartments (Supplementary Fig. 6g). To explore mitochondrial function and organization closer to the nucleus in naïve and RSV-infected A549 cells, we coupled 3D targeted cryo-FLM-FIB-milling with montage cryo-ET (Fig. 1, Supplementary Fig. 7). Low toxicity fluorescent nanoparticles (40 nm)[27] were internalized by the cells and used as FIB-milling “fiducials” to position and adjust milling boxes on-the-fly in the Z and XY planes based on the position of nanoparticles relative to the ROI in the 3D cryo-FLM Z-stack (Supplementary Figs. 7, 8b-c). A square of interest was identified (Fig. 1a) and milling boxes were initially positioned via external markers using 3DCT[9] and CorRelator[24] (Fig. 1b, Supplementary

Fig. 8c), then further adjusted based on the FIB-milling "fiducials" (Supplementary Fig. 8d-f) during the thinning process. Uniformly-sized nanoparticles can be readily differentiated from electron dense lipid droplets by SEM and cryo-ET (Fig. 1c, Supplementary Fig. 8j-m). Post correlation[28] of cryo-EM images of lamella with the corresponding pre-milling cryo-FLM section confirmed the locations of ROIs and nanoparticles (Fig. 1d-f, Supplementary Fig. 8h-i). We targeted fluorescently-labeled mitochondria-rich areas near the nucleus where multiple 3X3 montage cryo-ET fields were collected; each montage covering an area of ~7 x 5.5 $\mu m$ (representative 3X3 montage tile in cyan box, Fig. 1e). The 3D correlative targeting in combination with montage cryo-ET supported the precise acquisition of large FOVs of a FIB-thinned cellular lamella. Within the 3D volume, the arrangement of mitochondria, the Golgi, rough ER, and nuclear pore complex along the nuclear envelope was observed with potential to retrieve high-resolution structural information[12] (Fig. 1f).

Next, we applied montage cryo-ET to primary neurons grown on micropatterned cryo-TEM grids[29,30]. Coupling micropatterning with cryo-ET has proven to be valuable for directing cytoskeleton organization and understanding neural outgrowth[30]. Straight-line patterns were used to control neurite growth of primary *Drosophila melanogaster* neurons (Fig. 2a-c). Multiple montage tilt series were collected along neurites protruding from peripheral areas of the cell body (representative 3X4 montage site (~8 x 7 $\mu m$) delineated in Fig. 2d). The montage cryo-tomogram revealed the architecture of the cytoskeleton, including continuous microtubules (~9 $\mu m$) stretching along the pattern and the presence of actin filaments extending from the neurite. The localization and 3D organization of

mitochondria that exhibited matrix regions densely packed with calcium granules was indicative of possible metabolic activities[31] (Fig. 2e-f). The application of cryo-montage tomography is important for generating large-scale 3D molecular vistas of neurons and other cells that are responding to external physical cues such as those imposed by micropatterning.

A completely reconstructed unbinned tomogram of a fully stitched 3X4 montage tilt series could be ~700 GB or more, particularly as the sampling pixel size decreases and tile pattern size expands. To maximize output and develop efficient processing schemes, we explored sorting individual tile tilt series and independently reconstructing them into tile tomograms that have the same volume and pixel size as a regular single cryo-tomogram. Consistent with simulation results (Supplementary Figs. 4, 5), each tile tilt series exhibited the same spiral image shift trajectory as the fully-stitched montage tilt series (Supplementary Fig. 9a-b). When the largest image translation offset was restricted to 30% or less of the FOV per image, each tile tilt series maintained the specified ROI within the majority of the tilt series images. After determining the eucentric plane of the montage field, per tilt focus and per group tracking were adjusted using the nearby focus area during the dose-symmetric acquisition. CTF determination using CTFPLOTTER[32] indicated that the data acquisition scheme provided a relatively stable defocus ($\pm\ 1\ \mu m$) over tilt series acquired from a wide range of samples (Supplementary Fig. 9c). We used CTFFIND4 for tilted defocus determination[23]. CTFFIND4 reported the high-resolution limit of detected Thon rings that ranged from 8 to 20 $\text{Å}$ for individual tiles and stitched montages at 0° tilt and high tilts (Supplementary Fig. 9d). Per tile defocus adjustment could be

implemented to decrease defocus variation. We performed sub-tomogram averaging on the RSV F fusion (F) glycoprotein to compare with our previous results[33]. Viral F glycoproteins are arrayed on the surface of filamentous RSV particles either budding or released from RSV-infected BEAS-2B cells grown on EM grids (Supplementary Fig. 10a-e). Volumes containing F were extracted from individually-reconstructed tile tomograms for STA (n = 23250, ~29 Å, C3 symmetry imposed). In an effort to determine whether an improved sub-tomogram average would result from the removal of particles located along stitched overlap zones (15% of X and 10% of Y edges), 971 particles from those regions out of the 7947 total unique particles were removed to yield a refined average of F at ~26 Å resolution (n = 20707, C3 symmetry imposed). These averaged F structures were on par with what has been reported[33]. We anticipate further improvements to the average could be gained, in part, by using a lower defocus range, a larger number of particles, and further refinement of particles included in the average based upon position in individual tile tomograms.

In conclusion, correlative cryo-montage tomography is a workflow suited for capturing both comprehensive fields of view and targeted regions of interest in complex biological environments at molecular-level resolution. The montage cryo-ET tools presented here are applicable for modern TEMs with stable lens systems. Montage cryo-ET is adaptable to existing imaging routines and supports flexible user-defined tile patterns, streamlined data acquisition, pre-processing automation, and maximization of cryo-ET output with both individual tile and montage tilt series. Rectangular array tile montage for cryo-ET has laid the foundation for future developments with super-montage tomography that

incorporate both image-shift and stage-shift collection[17]. Cryo-ET tilt series are commonly acquired at the highest tolerable dose for the biological target; future work will assess the impact of total dose, dose distribution, and montage tile stitching on the preservation of high-resolution structural information for both montage and individual tile tomograms. Ultimately, montage tomography solutions will help bridge the resolution gap and field of view losses present between multi-modal microscopy imaging pipelines.

**Acknowledgements.** We thank Dr. Jill Wildonger, Dr. Sihui Z. Yang, and Mrs. Josephine W. Mitchell in the Department of Biochemistry, University of Wisconsin, Madison for kindly sharing the elav-Gal4, UAS-CD8 : GFP fly strain (Bloomington stock center, #5146). This work was supported in part by the University of Wisconsin, Madison, the Department of Biochemistry at the University of Wisconsin, Madison, and public health service grants R01 GM114561 and U24 GM139168 to E.R.W. from the NIH. We are grateful for the use of facilities and instrumentation at the Cryo-EM Research Center in the Department of Biochemistry at the University of Wisconsin, Madison.

**Author contributions.** J.E.Y. and E.R.W. conceived and designed the study. M.R.L, J.E.Y, E.R.W developed TomoGrapher and pre-processing workflow. J.E.Y., B.S.S, J.Y.K., D.P., J.M.S., V.P., A.K., K.C., A.K., K.T. prepared the samples, performed the experiments, and data processing. J.E.Y. and E.R.W. wrote the manuscript, with contributions from all authors. All authors read and approved the manuscript.

**Competing Interests.** The funders had no role in study design, data collection and interpretation, or the decision to submit the work for publication. The authors declare no competing financial or non-financial interests.

## References


1 Kühlbrandt, W. The Resolution Revolution. *Science* **343**, 1443-1444, doi:10.1126/science.1251652 (2014).

2 Turk, M. & Baumeister, W. The promise and the challenges of cryo-electron tomography. *FEBS Letters* **594**, 3243-3261, doi:https://doi.org/10.1002/1873-3468.13948 (2020).

3 Thompson, R. F., Walker, M., Siebert, C. A., Muench, S. P. & Ranson, N. A. An introduction to sample preparation and imaging by cryo-electron microscopy for structural biology. *Methods* **100**, 3-15, doi:10.1016/j.ymeth.2016.02.017 (2016).

4 Kiss, G. *et al.* Structural analysis of respiratory syncytial virus reveals the position of M2-1 between the matrix protein and the ribonucleoprotein complex. *J Virol* **88**, 7602-7617, doi:10.1128/jvi.00256-14 (2014).

5 Schur, F. K. M. Toward high-resolution in situ structural biology with cryo-electron tomography and subtomogram averaging. *Curr. Opin. Struct. Biol.* **58**, 1-9, doi:https://doi.org/10.1016/j.sbi.2019.03.018 (2019).

6 Al-Amoudi, A. *et al.* Cryo-electron microscopy of vitreous sections. *EMBO J* **23**, 3583-3588, doi:10.1038/sj.emboj.7600366 (2004).

7 Rigort, A. *et al.* Micromachining tools and correlative approaches for cellular cryo-electron tomography. *J. Struct. Biol.* **172**, 169-179, doi:https://doi.org/10.1016/j.jsb.2010.02.011 (2010).

8 Hampton, C. M. *et al.* Correlated fluorescence microscopy and cryo-electron tomography of virus-infected or transfected mammalian cells. *Nat. Protoc.* **12**, 150-167, doi:10.1038/nprot.2016.168 (2017).

9 Arnold, J. *et al.* Site-Specific Cryo-focused Ion Beam Sample Preparation Guided by 3D Correlative Microscopy. *Biophys. J.* **110**, 860-869, doi:https://doi.org/10.1016/j.bpj.2015.10.053 (2016).

10 Phan, S., Terada, M. & Lawrence, A. Serial reconstruction and montaging from large-field electron microscope tomograms. *Annu Int Conf IEEE Eng Med Biol Soc* **2009**, 5772-5776, doi:10.1109/IEMBS.2009.5332531 (2009).

11 Iancu, C. V. *et al.* A “flip–flop” rotation stage for routine dual-axis electron cryotomography. *J. Struct. Biol.* **151**, 288-297, doi:https://doi.org/10.1016/j.jsb.2005.07.004 (2005).

12 Shannon, C. E. Communication in the Presence of Noise. *Proceedings of the IRE* **37**, 10-21, doi:10.1109/JRPROC.1949.232969 (1949).

13 Faruqi, A. R. & McMullan, G. Direct imaging detectors for electron microscopy. *Nuclear Instruments and Methods in Physics Research Section A: Accelerators, Spectrometers, Detectors and Associated Equipment* **878**, 180-190, doi:https://doi.org/10.1016/j.nima.2017.07.037 (2018).

14 Baldwin, P. R. *et al.* Big data in cryoEM: automated collection, processing and accessibility of EM data. *Current Opinion in Microbiology* **43**, 1-8, doi:10.1016/j.mib.2017.10.005 (2018).

15 Peck, A. *et al.* Montage electron tomography of vitrified specimens. *bioRxiv*, 2021.2011.2002.466666, doi:10.1101/2021.11.02.466666 (2021).

16 Chen, R. *et al.* EPiK-a Workflow for Electron Tomography in Kepler. *Procedia Comput Sci* **20**, 2295-2305, doi:10.1016/j.procs.2014.05.214 (2014).

17 Mastronarde, D. N., van der Heide, P. A., Morgan, G. P. & Marsh, B. J. Supermontaging: Reconstructing Large Cellular Volumes by Stitching Together Laterally Adjacent Tomograms. *Microsc Microanal.* **14**, 106-107, doi:10.1017/S1431927608086820 (2008).

18 Phan, S. *et al.* TxBR montage reconstruction for large field electron tomography. *J. Struct. Biol.* **180**, 154-164, doi:https://doi.org/10.1016/j.jsb.2012.06.006 (2012).

19 Mastronarde, D. N. Automated electron microscope tomography using robust prediction of specimen movements. *J. Struct. Biol.* **152**, 36-51, doi:10.1016/j.jsb.2005.07.007 (2005).

20 Fukushima, K., Kawakatsu, H. & Fukami, A. Fresnel fringes in electron microscope images. *Journal of Physics D: Applied Physics* **7**, 257-266, doi:10.1088/0022-3727/7/2/310 (1974).

21 Cope, J., Heumann, J. & Hoenger, A. Cryo-electron tomography for structural characterization of macromolecular complexes. *Curr Protoc Protein Sci* **Chapter 17**, Unit17.13-Unit17.13, doi:10.1002/0471140864.ps1713s65 (2011).

22 Kremer, J. R., Mastronarde, D. N. & McIntosh, J. R. Computer Visualization of Three-Dimensional Image Data Using IMOD. *J. Struct. Biol.* **116**, 71-76, doi:https://doi.org/10.1006/jsbi.1996.0013 (1996).

23 Bouvette, J. *et al.* Beam image-shift accelerated data acquisition for near-atomic resolution single-particle cryo-electron tomography. *Nat. Commun.* **12**, 1957, doi:10.1038/s41467-021-22251-8 (2021).

24 Yang, J. E., Larson, M. R., Sibert, B. S., Shrum, S. & Wright, E. R. CorRelator: Interactive software for real-time high precision cryo-correlative light and electron microscopy. *J Struct Biol*, 107709, doi:10.1016/j.jsb.2021.107709 (2021).

25 Hu, M. *et al.* Respiratory syncytial virus co-opts host mitochondrial function to favour infectious virus production. *eLife* **8**, e42448, doi:10.7554/eLife.42448 (2019).

26 Ke, Z. *et al.* The Morphology and Assembly of Respiratory Syncytial Virus Revealed by Cryo-Electron Tomography. *Viruses* **10**, doi:10.3390/v10080446 (2018).

27 Bahadar, H., Maqbool, F., Niaz, K. & Abdollahi, M. Toxicity of Nanoparticles and an Overview of Current Experimental Models. *Iran Biomed J* **20**, 1-11, doi:10.7508/ibj.2016.01.001 (2016).

28 Klein, S. *et al.* Post-correlation on-lamella cryo-CLEM reveals the membrane architecture of lamellar bodies. *Communications Biology* **4**, 137, doi:10.1038/s42003-020-01567-z (2021).

29 Toro-Nahuelpan, M. *et al.* Tailoring cryo-electron microscopy grids by photo-micropatterning for in-cell structural studies. *Nat. Methods* **17**, 50-54, doi:10.1038/s41592-019-0630-5 (2020).

30 Sibert, B. S., Kim, J. Y., Yang, J. E. & Wright, E. R. Micropatterning Transmission Electron Microscopy Grids to Direct Cell Positioning within Whole-Cell Cryo-Electron Tomography Workflows. *JoVE*, e62992, doi:doi:10.3791/62992 (2021).

31 Wolf, S. G. *et al.* 3D visualization of mitochondrial solid-phase calcium stores in whole cells. *eLife* **6**, e29929, doi:10.7554/eLife.29929 (2017).

32 Xiong, Q., Morphew, M. K., Schwartz, C. L., Hoenger, A. H. & Mastronarde, D. N. CTF determination and correction for low dose tomographic tilt series. *J. Struct. Biol.* **168**, 378-387, doi:10.1016/j.jsb.2009.08.016 (2009).

33 Stobart, C. C. *et al.* A live RSV vaccine with engineered thermostability is immunogenic in cotton rats despite high attenuation. *Nat. Commun.* **7**, 13916, doi:10.1038/ncomms13916 (2016).

**Methods section only**

34 Egger, B., van Giesen, L., Moraru, M. & Sprecher, S. G. In vitro imaging of primary neural cell culture from Drosophila. *Nat. Protoc.* **8**, 958-965, doi:10.1038/nprot.2013.052 (2013).

35 Lu, W., Lakonishok, M. & Gelfand, V. I. Kinesin-1-powered microtubule sliding initiates axonal regeneration in Drosophila cultured neurons. *Mol. Biol. Cell* **26**, 1296-1307, doi:10.1091/mbc.E14-10-1423 (2015).

36 Bieber, A., Capitanio, C., Wilfling, F., Plitzko, J. & Erdmann, P. S. Sample Preparation by 3D-Correlative Focused Ion Beam Milling for High-Resolution Cryo-Electron Tomography. *JoVE*, e62886, doi:doi:10.3791/62886 (2021).

37 Wagner, F. R. *et al.* Preparing samples from whole cells using focused-ion-beam milling for cryo-electron tomography. *Nat. Protoc.* **15**, 2041-2070, doi:10.1038/s41596-020-0320-x (2020).

38 Gorelick, S. *et al.* PIE-scope, integrated cryo-correlative light and FIB/SEM microscopy. *eLife* **8**, e45919, doi:10.7554/eLife.45919 (2019).

39 Reisinger, T., Leufke, P. M., Gleiter, H. & Hahn, H. On the relative intensity of Poisson's spot. *New Journal of Physics* **19**, 033022, doi:10.1088/1367-2630/aa5e7f (2017).

40 Weis, F., Hagen, W. J. H., Schorb, M. & Mattei, S. Strategies for Optimization of Cryogenic Electron Tomography Data Acquisition. *JoVE*, e62383, doi:doi:10.3791/62383 (2021).

41 Zheng, S. Q. *et al.* MotionCor2: anisotropic correction of beam-induced motion for improved cryo-electron microscopy. *Nat. Methods* **14**, 331-332, doi:10.1038/nmeth.4193 (2017).

42 Mastronarde, D. N. & Held, S. R. Automated tilt series alignment and tomographic reconstruction in IMOD. *J Struct Biol* **197**, 102-113, doi:10.1016/j.jsb.2016.07.011 (2017).

43 Grant, T. & Grigorieff, N. Measuring the optimal exposure for single particle cryo-EM using a 2.6 Å reconstruction of rotavirus VP6. *eLife* **4**, e06980, doi:10.7554/eLife.06980 (2015).

44 Moreno, J. J., Martínez-Sánchez, A., Martínez, J. A., Garzón, E. M. & Fernández, J. J. TomoEED: fast edge-enhancing denoising of tomographic volumes. *Bioinformatics* **34**, 3776-3778, doi:10.1093/bioinformatics/bty435 (2018).

45 Chen, M. *et al.* Convolutional neural networks for automated annotation of cellular cryo-electron tomograms. *Nat. Methods* **14**, 983-985, doi:10.1038/nmeth.4405 (2017).

46 Rohou, A. & Grigorieff, N. CTFFIND4: Fast and accurate defocus estimation from electron micrographs. *J. Struct. Biol.* **192**, 216-221, doi:https://doi.org/10.1016/j.jsb.2015.08.008 (2015).

47 Nicastro, D. *et al.* The molecular architecture of axonemes revealed by cryoelectron tomography. *Science* **313**, 944-948, doi:10.1126/science.1128618 (2006).

48 Liljeroos, L., Krzyzaniak, M. A., Helenius, A. & Butcher, S. J. Architecture of respiratory syncytial virus revealed by electron cryotomography. *Proc Natl Acad Sci USA* **110**, 11133, doi:10.1073/pnas.1309070110 (2013).

381 49 McLellan Jason, S. *et al.* Structure of RSV Fusion Glycoprotein Trimer Bound to a
382 Prefusion-Specific Neutralizing Antibody. *Science* **340**, 1113-1117,
383 doi:10.1126/science.1234914 (2013).
384 50 Pettersen, E. F. *et al.* UCSF Chimera--a visualization system for exploratory research and
385 analysis. *J Comput Chem* **25**, 1605-1612, doi:10.1002/jcc.20084 (2004).
386

387

## Methods.

**Cell lines and cell culture.** HeLa cells (ATCC CCL-2, ATCC, Manassas, VA, USA) and A549 cells (ATCC, CCL-185) were cultured and maintained in supplemented DMEM complete medium and BEAS-2B cells (ATCC, CRL-9609) cultured in supplemented RPMI-1640 complete medium as reported previously[26]. Primary *Drosophila melanogaster* third-instar larval neurons (the strain elaV-Gal4, UAS-CD8::GFP maintained and kindly provided by the Wildonger lab, UCSD) were extracted, cultured in supplemented Schneider's media, and maintained on micropatterned grids as previously described[34].

**Cell seeding, infection and *in-situ* labeling on TEM grids.** Cell seeding on the TEM grids was performed following previous reports[26]. Briefly, Quantifoil grids (200 mesh Au R2/2 carbon or $SiO_2$ film; Quantifoil Micro Tools GmbH, Großlöbichau, Germany) were coated with extra carbon (5 to 8 nm) and glow discharged (10 mA, 60 sec). HeLa and BEAS-2B cells were trypsinized and seeded at a density of 0.7 X $10^5$ cells/mL, followed by an overnight incubation prior to subsequent applications. For montage cryo-ET and correlative cryo-FLM-montage-ET, HeLa and BEAS-2B cells on the grids were infected with the recombinant virus strain RSV rA2-m$K^+$ at an optimized multiplicity of infection (M.O.I.) of 10 for 24 hours at 37 °C and 5 % $CO_2$, as determined previously[26]. For cryo-focused ion beam milling (FIB-milling), A549 cells were digested and seeded at a density of 0.3 X $10^5$ cells/mL on $SiO_2$ Au Quantifoil grids for 16 to 24 hours.

**Micropatterning and neuron cell culture on TEM grids.** Micropatterning and culturing of primary *Drosophila* larval neurons was performed as described[30]. Briefly, the extra

carbon coated gold Quantifoil grids (200 mesh, R 1.2/20, holey carbon film; Quantifoil Micro Tools GmbH, Großlöbichau, Germany) were glow-discharged, and coated with 0.05% poly-L-Lysine (PLL). The grids were then functionalized by applying a layer of anti-fouling polyethylene glycol-succinimidyl valerate (PEG-SVA), followed by application of a photocatalyst reagent, 4-benzoylbenzyl-trimethylammonium chloride (PLPP) gel. Maskless photopatterning was performed to ablate the anti-fouling layer in defined patterns with a UV laser ($\lambda$ = 375 nm, at a dose of 30 mJ/mm$^2$) using an Alvéole PRIMO micropatterning system. Adherent extracellular matrix (ECM) protein, fluorescently-labeled concanavalin A, Alexa Fluor™ 350 conjugate (emission, $\lambda$ = 457 nm, 0.5 mg/mL in water or PBS, ThermoFisher Scientific), was then added to promote the cellular adhesion and growth of primary *Drosophila* larval neurons isolated and cultured according to established protocols[34,35]. These neurons had pan-neuronal GFP expression (emission, $\lambda$ = 525 nm) on the membrane (CD8-GFP) to allow for tracking using live-cell wide-field fluorescent microscopy imaging. Neurons on patterned grids grew for a minimum of 48-72 hours for neurite growth prior to plunge freezing.

**Vitrification.** For EM grids prepared for non-FIB cryo-ET applications, 4 μl of 10 nm BSA-treated gold fiducial beads (Aurion Gold Nanoparticles, Electron Microscopy Sciences, PA, USA) were applied before vitrification. The grids were plunge-frozen using either a Gatan CryoPlunge3 system (CP3) with GentleBlot blotters (Gatan, Inc., Pleasanton, CA, USA) or a Leica EM GP (Leica Microsystems). The Gatan CP3 system was operated at 75 ~ 80 % humidity and a blot time of 4.5 to 5.5 s for double-sided blotting and plunge freezing. The Leica EM GP plunger was set to 25 °C to 37 °C, 99% humidity and blot

434 times of 6 s for R 1.2/20 micropatterned carbon-foil grids, and 15 s for R2/2 $SiO_2$ foil grids
435 for single-sided blotting and plunge freezing. Plunge-frozen grids were then clipped and
436 stored in cryo-grid boxes under liquid nitrogen.
437
438 **Correlative live-cell and cryogenic fluorescent microscopy.** Healthy A549 or RSV-
439 infected HeLa cells were stained with MitoTrackerGreen FM (M7514, ThermoFisher
440 Scientific, 100 nM, 30 min at 37 °C and 5 % $CO_2$), washed, and stained with Hoechst-
441 33342 (H3570, ThermoFisher Scientific, 1 to 1000 dilution, 20 min at 37 °C and 5 % $CO_2$)
442 to visualize mitochondria and the nucleus. As reported previously[8], live-cell wide-field
443 imaging (20 X, 0.4NA lens, dry) and cryo-FLM (50 X, ceramic-tipped, 0.9NA lens) on
444 vitrified samples were performed on a Leica DMi8 and Leica EM Cryo-CLEM THUNDER
445 system, respectively. The brightfield and band pass filter cubes of GFP (emission, λ =
446 525 nm), DAPI (emission, λ = 477 nm), Texas Red (emission, λ = 619 nm), and Y5
447 (emission, λ = 660 nm) were used. Live-cell wide-field images were collected as a grid
448 montage at 20X. For cryo-FLM, Z-stack projections of 12 to 15 $\mu m$ for each channel were
449 collected on the vitrified sample at a Nyquist sampling step of 350 nm using the Leica
450 LAS X software. Small Volume Computational Clearance (SVCC) from the Leica LAS X
451 THUNDER package was applied for fluorescent image deconvolution and blurring
452 reduction on the cryo-FLM image stacks. All images and mosaics were exported and used
453 as LZW compressed lossless 16-bit TIFF format. The on-the-fly cryo-FLM to cryo-ET
454 correlation and data collection was performed using CorRelator[24]. Grids that were imaged
455 under cryogenic conditions were saved and stored in in cryo-grid boxes under liquid
456 nitrogen.

457

458 **3D targeted Cryo-FIB-SEM.** Low toxic nanoparticles of 40 nm (FluoSpheres, carboxylate
459 modified microsphere, dark red fluorescent (660/680 nm), ThermoFisher Scientific,
460 F8789) were introduced to cells seeded on the grid for an incubation of 2 hours at 2
461 mg/mL, followed by washing with 1X PBS and 5 min incubation of 5 ~10 % glycerol as a
462 cryoprotectant to properly vitrify cells. Afterwards, 4 μl of diluted 200 nm FluoSpheres (1
463 to 200 dilution, dark red fluorescent (660/670 nm), ThermoFisher Scientific, F8807) were
464 applied to the grid in the humidity chamber of the Leica EM GP plunger prior to the
465 vitrification step. Following Leica EM Cryo CLEM THUNDER imaging, clipped grids were
466 transferred into a dual-beam (SEM/FIB) Aquilos2 cryo-FIB microscope (ThermoFisher
467 Scientific) operating under cryogenic conditions. To improve the sample conductivity and
468 reduce the curtaining artifacts during FIB milling, the grid was first sputter-coated with
469 platinum (10 mA, 15 to 30 sec), and then coated with organometallic platinum using the
470 in-chamber gas injection system (GIS, 6 sec with a measured deposition rate of 600
471 nm/sec). A 2D affine transformation on the XY plane was performed to align cryo-FLM
472 and cryo-scanning electron microscopy (SEM) grid mosaics on a rough micron scale and
473 to further correlate square images from two modalities on a fine nanometer scale
474 precision using hole centroids or 200 nm FluoSpheres in CorRelator. The eucentric height
475 of the region of interest on the cryo-shuttle inside the dual-beam microscope and a
476 shallow FIB-milling angle of 8 to 12° were determined. 2D SEM and FIB views of the
477 squares (with the field of view large enough to include sufficient external microspheres
478 and features as registration points) that contained the region of interest (ROI) were
479 collected at the eucentric height and milling angle. 3D coordinate transform between the

3D Z-stack of the Y5 channel (nanoparticles, emission λ = 680 nm) and the 2D FIB view was conducted through the optimized rigid body 3D transformation algorithm available in the 3DCT package using external 200 nm FluoSpheres (n = 4 to 10) as registration points[36]. The transformed coordinates (X, Y, Z) were then imported into CorRelator to fine tune the deviations in X and Y coordinates introduced by the Z transformation in 3DCT, using the closed-form best-fitting least-square solution. The FIB milling boxes were positioned based on the prediction in the 2D FIB view in CorRelator[24]. The ion-beam milling process was performed using 0.3 nA for rough milling and gradually decreased currents of 0.1 nA, 50 pA, 30 pA, and 10 pA, following previously established protocols[37]. Without changing the sample/shuttle position during the milling, a series of cryo-SEM images (electron beam set at 2 kV, 25 pA, dwell time of 1 μs) were collected as the lamella was thinned from an initial thickness of 5 μm, 3 μm, 1 μm, to 800 nm, 500 nm and to the final 200 nm. The SEM images were used to: 1) check the milling process related to stage drift, lamella bending, etc., 2) adjust the milling positions by visualizing the density of internalized 40 nm nanoparticles on the lamella and comparing their positions (X, Y in ~100 to 200 nm deviation error, and 500 nm in Z relative to the ROI ) in the correlated FLM Z-stack, and 3) to confirm the successfully milled isolated region houses the ROI. On-the-fly monitoring of nanoparticle presence provided quick and movement-free feedback on 3D targeted milling when an integrated FLM system is not available. It could also help eliminate excessive alignment steps introduced by shuttle moving in an integrated FLM and FIB-SEM system when the sample is moved back and forth between the FLM imaging and FIB-SEM positions[38].

503 To further confirm the preservation of an ROI in the lamella, lamella were transferred to
504 the Leica EM Cryo-CLEM THUNDER system and a Z-stack of the same channels was
505 collected. Post-correlations on lamella of cryo-FLM, cryo-SEM, and cryo-EM were
506 performed using angle-corrected neighboring signals around the lamella to transform
507 cryo-FLM signals to corresponding features on the lamella under cryo-SEM and cryo-EM
508 as described previously[28].
509
510 **Cryo-electron tomography and reconstructions.** After live-cell FLM, cryo-FLM
511 imaging, and/or cryo-FIB milling, the same clipped frozen grids were imaged using a Titan
512 Krios (ThermoFisher Scientific, Hillsboro, OR, USA) at 300 kV. Images were acquired on
513 a Gatan Bioquantum GIF-K3 camera in EFTEM mode using a 20 eV slit. Images were
514 captured at various magnifications of 81x (4485 Å/pixel) for whole grid mosaic collection,
515 470x (399 Å/pixel) and 1950x (177.6 Å/pixel) for square or whole lamella overview, 6500x
516 (27.4 Å/pixel) for intermediate magnification imaging where the field of view is suitable for
517 reliable tracking and 40 nm nanoparticles are visibly distinguished, and 19500x (4.603
518 Å/pixel) for data acquisition using the SerialEM software package[19]. The full frame size of
519 5760 x 4092 pixels (counting, CDS mode at 10 eps of dose rate) was collected.
520
521 *Montage cryo-ET setup in SerialEM*. Regular image-shift montage acquisition and the
522 multiple record function in SerialEM were adapted for implementation of overlapped
523 beam-image shift tiling. Benchmarks were done at a data acquisition magnification (pixel
524 size of 4.603 Å/pixel) typical for cryo-ET. The illuminated area of 3.1 μm in diameter on
525 the sample was determined by the beam size on the camera and the lens magnification.

Fresh gains were collected with this beam size (3.1 μm) and the gain normalized image over vacuum was low pass filtered to 50 Å to enhance the signal of Fresnel fringe peaks. Based on the behaviors of Fresnel fringes[39] and EM Gaussian signal distribution, the intensity value of the image over pixel was fitted into two distribution curves, a Poisson curve (maximum likelihood estimate/peak $\lambda$) to fit the edge areas considered as "signal peaks" using 20% of X and Y dimension extending from the edge towards the center, and a Gaussian curve ($\mu \pm 2\sigma$) to fit the center area considered as noise/background using 90% of whole X and Y dimension from the center towards the edge with a 10% overlap with the "edge" area in MatLab (*poissfit* and *gaussianFit* Curve Fitting Toolbox, MathWorks, Natick, MA, USA). The cut-off from "signal" to "noise" were determined as the possibility of "signal" peaks fading into $\mu \pm 2\sigma$ of "noise" distribution. From multiple measurements ($n \geq 3$) along the circular beam edge, the cut-off was 3.5 ~4 % of X extending from the edge and insignificant in the Y direction. Thus, the rest of the image was considered as a fringeless FOV. Over a wide range of samples, we selected the pixel overlaps of 15% to 20% in the fringe-affected X-direction and 10% in the fringe-free Y-direction as the optimal tiling strategy, such that the usable field of view per camera frame was maximized after correction of Fresnel fringes and optimization of the pre-exposed area outside of camera frame FOV. A regular montage with minimum dimensions of 2X2 was collected with the designated overlaps in X and Y at the data acquisition magnification. A rigorous and reliable image shift calibration in SerialEM at the data acquisition magnification was performed and repeated to ensure a more accurate shift. The beam-image shift tiling information (ImageShift entry under each item section in the image metadata file ".mdoc" file) was obtained on-the-fly. The shift in the X direction to

549 achieve the frame overlap of 15 % in X was retrieved by calculating the difference in
550 image shift between the tile 1 (PieceCoordinates of 0 0 0) and tile 3 (PieceCoordinates of
551 4608 0 0). The shift in the y direction to achieve the frame overlap of 10 % overlap in Y
552 was retrieved by calculating the difference between tile 1 (PieceCoordinates of 0 0 0) and
553 tile 2 (PieceCoordinates of 0 3516 0). The MultishotParams (X/Y component of image
554 shift vector) was subsequently modified to reflect the tile montage image shift and saved
555 under the SerialEM setting file.
556
557 *Montage cryo-tilt series collection in SerialEM*. A SerialEM macro (available at
558 https://github.com/wright-cemrc-projects/cryoet-montage) was used to implement the
559 montage tilt series by acquiring overlapping tiles with designated overlaps to form a
560 montage at each tilt with an additional translational shift and or rotation shift to distribute
561 the dose. Autofocusing was performed at each tilt and shifted along the orientation of the
562 tilt axis 500 nm plus the maximum translational shift of the center of montage tile pattern
563 (e.g. 0.8 µm, Supplementary Figs. 9a) away from the edge of the montage tile pattern.
564 The total dose per tile tilt series was 30-40% below the maximum dose the sample was
565 able to tolerate before evidence of punctate bubbles. At the beginning of each grouped
566 tilt, high magnification/data acquisition tracking with a threshold of 5% of the FOV to
567 acquire a new tracking reference and to iterate the alignment until the threshold was met
568 (usually within one or two iterations), using the nearby autofocusing area, was performed.
569 An additional lower intermediate magnification tracking on a larger FOV of the region of
570 interest was implemented when the tilt angles were above 30°, with a threshold of a
571 difference greater than 10% (usually within one or two iterations). The tilt series collection

was paused when the iterations for convergence exceeded 5 times. Benchmarks were done using a 3X3 or 3X4 montage tile pattern and a dose-symmetric scheme running at ± 51° with 3° increments, groups of 3 tilts (original "Hagen scheme" is group of 1 tilt) and a dose of 2 $e^-/Å^2$/tile per tilt for RSV-infected BEAS-2B and HeLa cells, and neurons on micropatterned grids, while a dose of 1.42 $e^-/Å^2$/tile per tilt for A549 cell lamella based on the dose tolerance measurements of each sample. The CDS counting mode and dose rate of 10 eps were used on a K3 camera. The translational shift off-sets followed the global spiral displacement ($A_{final}$ = 1.5, Period = 3, Turns = 50, Revolutions = 15 as input parameters to control the spiral size and resulting displacement offsets). The speed of collection varied with the size of the montage tile, the type of microscope, detector used and sample-dependent total dose. Benchmark collections were 60 min on average and rendered 9 sub-tilt series (3X3 tile pattern) that were stitched seamlessly to form one montaged tilt series. Translational spiral off-sets and collection schemes (bidirectional, dose-symmetric, defocus, etc.) can be adjusted accordingly in the SerialEM macro. The SerialEM macro can be modified to adjust translational spiral off-sets and collection schemes (bidirectional, dose-symmetric, defocus, etc.). The macro can be integrated into existing common automated data collection schemes using the function *Navigator Acquire at points* in SerialEM[40].

*Montage tilt series processing*. All movie frames per acquisition (0.1~0.2 $e^-/Å^2$/frame) were aligned and corrected using MotionCor2[41]. For montage tilt series, the total tiles per tilt were registered and stitched together using the designated beam coordinates supplied to the microscope as described above and with linear cross-correlation methods[42].

Despite the fringes on the edge, intrinsic low contrast and low dose received by cryo-tilt series, the regularity of the montage tiling pattern and sufficient overlaps with optimized tiling strategy consistently provided robust and automated seamless stitching without user intervention up to $\pm$ 39°. Manual image alignment (MIDAS), implemented in the IMOD package[42], was used to adjust piece coordinates and iteratively cross-correlate adjacent tiles at higher tilts when necessary. Fully stitched montage tilt series were binned by 2. Tilt series alignment and tomographic reconstructions were performed using the IMOD package with a final pixel size of 9.206 Å. In the absence of gold fiducials in the FIB-milled lamella, alignment of the tilt series was performed using patch tracking or internalized nanoparticles as tracking markers. CTF correction using ctfplotter and ctfphaseflip and dose-weighted filtering[43] were applied to the aligned tilt series prior to tomogram reconstruction. For segmentation, the aligned tilt series were further binned 3X (final pixel size of 27.6 Å, binned 6X) prior to the tomogram reconstruction. Tomograms were either processed using fast edge-enhancing denoising algorithm based on anisotropic nonlinear diffusion implemented in TomoEED[44] or Gaussian low-pass filtered to 80 Å for visualization and segmentation. Tomograms of stitched montage tilt series (final pixel size of 27.6 Å) were annotated using convolutional neural networks implemented in the EMAN2 package[45]. For the sub-tilt series, motion-corrected frames were sorted to generate individual tile tilt series that were CTF estimated using CTFFIND4[46]. Tilt series that contained one or more inadequate projections (not properly tracked or failed CTF estimation) were discarded. Qualified sub-tilt series were then aligned, CTF corrected with ctfplotter and ctfphaseflip, dose-weighted filtered, binned to 2X (a final pixel size of 9.206 Å), and reconstructed into tomograms, similar to stitched montage tilt series

618 implemented in the IMOD package. Python or bash scripts (available at
619 https://github.com/wright-cemrc-projects/cryoet-montage) were used to automate the
620 movie frame alignment, montage tile stitching, sub-tilt and montage tilt generation.
621
622 **Sub-tomogram averaging.** For proof of concept, all averaging was done on unfiltered
623 sub-tilt tomograms using PEET 1.15.0[47], following the steps reported previously[33].
624 Particles were manually picked from low pass filtered sub-tilt tomograms binned 2X to a
625 final pixel size of 9.206 Å. Initial particle orientation and rotation axes of particles were
626 generated using SpikeInit (PEET). An initial alignment was done with 565 particles from
627 one tomogram using post-fusion F glycoprotein (EMDB-2393)[48] low pass filtered to 60 Å
628 as the initial reference. The final average from this first run was low pass filtered to 60 Å
629 and used as the initial reference for a second run on 12,435 particles from a total of 12
630 sub-tilt tomograms, with a soft-edged cylinder mask applied during the alignment.
631 Duplicate particles were removed during each iteration with a tolerance of 73.6 Å (8
632 voxels). An additional iteration was done with refined particles using a smaller search
633 range and a larger mask with softer edges. The final average from the second run
634 suggested a three-fold symmetry, consistent with reported crystal structures[49]. C3
635 symmetry was imposed using *modifyMotiveList* in PEET to generate a three-fold
636 symmetric data set. The C3 symmetric data set was aligned and averaged using the final
637 average from the second run, low-pass filtered to 60 Å as the initial reference for
638 refinement with a smaller search range. The final sub-tomogram average (final pixel size
639 of 9.26 Å, binned 2X) from the C3 symmetry expanded particles was reconstructed from
640 23,259 particles. The final density map of F was low pass filtered to 29.53 Å based on the

641 FSC cutoff of 0.5 that was calculated in PEET. The picked particles that were in the
642 stitched area (15% in X and 10% in Y) were removed and the rest were reprocessed
643 following the same steps. The final sub-tomogram average (final pixel size of 9.26 Å,
644 binned 2X) from the C3 symmetry expanded particles was reconstructed from 20,707
645 particles. The final density map of F was low pass filtered to 27 Å based on the FSC cutoff
646 of 0.5 calculated in PEET. The atomic crystal model of pre-fusion F trimer (PDB: 4JHW)[49]
647 was fitted in the filtered electron density map in Chimera[50].
648
649 **TomoGrapher development.**
650 Simulations of the tiled montage imaging and electron beam exposures on a sample were
651 developed as a collection of C# classes built on the Unity 3D engine (version
652 2020.3.20f1). The simulation represents an array of M x N x O volumes called voxels as
653 a sample interacted by an electron beam. The canvas “stage” comprises of 150 x 150
654 voxels (X = Y = 150, Z = 1, total extent of 10 x 10 x 0.2 μm) with the center butterfly ROI
655 spanning across 5 x 4 μm on the imaging XY plane. An interactive GUI describes
656 parameters of the imaging including sampling pixel spacing, illuminated area of the beam
657 on the camera, the tiling pattern of the beam, tilt ranges, and translations defined by spiral
658 offsets. A complete run of a simulation iterates through each tilt increment across the
659 range, and ray traces from a sampling position of the illuminated area in the direction of
660 the beam to find intersections on the stage of voxel volumes. Voxels intersected by the
661 rays are aggregated in a set, and each voxel in the set has its total dose incremented
662 once per beam. The viewer provides a real-time animation of the beam shifts, tilting of

663 the stage, and overall exposure at each voxel. TomoGrapher release versions and source
664 code are available at https://github.com/wright-cemrc-projects/cryoet-montage .
665
666 **Statistics and Reproducibility.** Experiments performed in Figs. 1b-e, 2a-b,
667 Supplementary Figs. 2, 3b-c, 6, 8, 9 were performed independently three times with
668 similar results. Experiments from Figs. 1f, 2c-f, were performed in duplicates, resulting in
669 7 montaged tilt series on FIB lamellas from two lamellas on two different grids and 13
670 montaged tilt series on two different micropatterned neuron grids.

## Figures and Legends

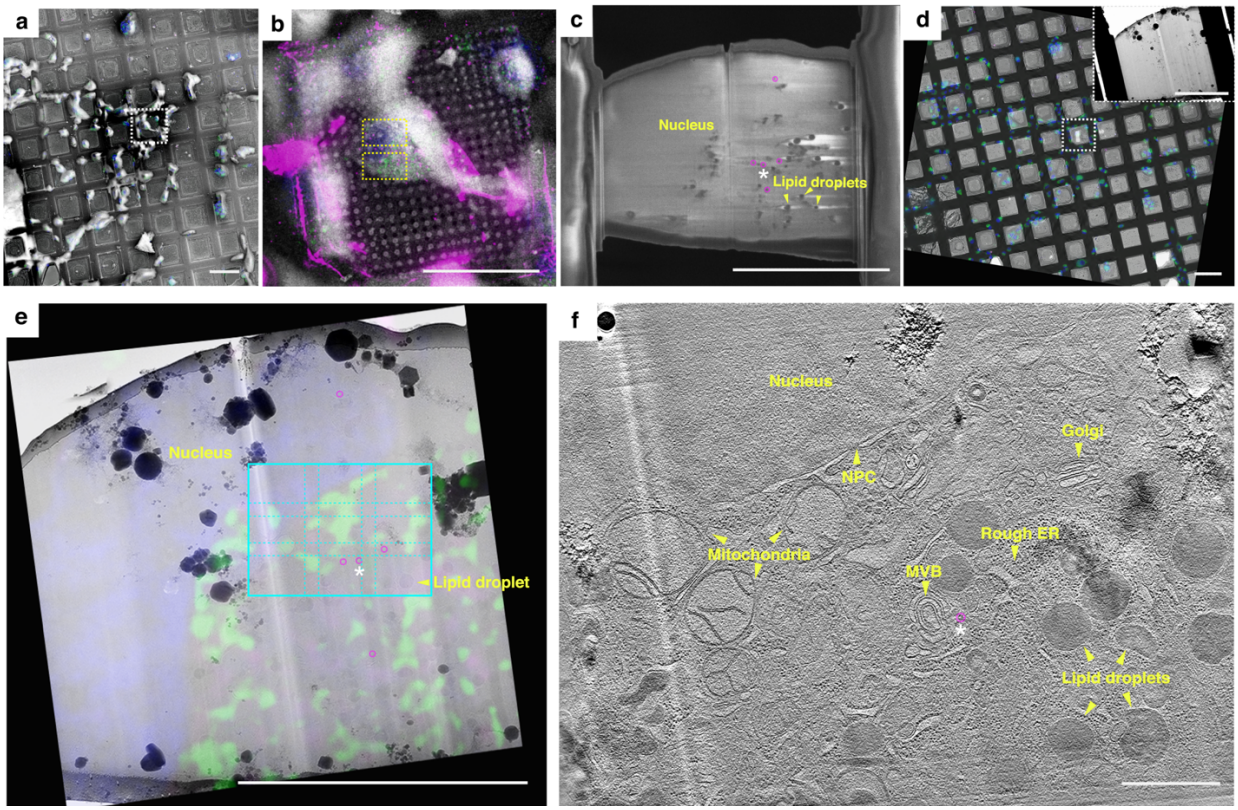


**Fig. 1. Correlative cryo-FLM, cryo-FIB-SEM, and montage cryo-ET of a cryo-lamella from an A549 cell to visualize the in-situ architecture of the nucleus, mitochondria, and other organelles. a.** Correlation of cryo-SEM and cryo-FLM grid mosaics to identify an A549 cell in the square of interest (white box). Scale bar, 100 $\mu m$. **b.** Cryo-FIB-milling boxes (pair of dashed yellow boxes) positioned to target the nucleus (blue) and mitochondria (green) in an A549 cell (white box in **a**), with internalized fluorescent beads (40 nm, pink) as milling "fiducials" for on-the-fly 3D targeted correlation. **c.** Cryo-SEM of the 200 nm thick lamella. Nucleus, lipid droplets, and internalized fluorescent beads (pink circles) are noted. Scale bars, 10 $\mu m$ in **b** and **c. d.** Correlation of pre-FIB-milled cryo-FLM and post-FIB-milled cryo-TEM grid mosaics (Inset, cryo-TEM image of the lamella at higher magnification). Scale bars, 100 $\mu m$ in **d**, 10 $\mu m$ in inset of **d**. **e.** Post correlation overlay of the 2D cryo-EM image of the lamella with the corresponding Z section from the pre-FIB-milled cryo-FLM stack. A 3x3 tiling for montage cryo-ET (cyan, 6.8 x 5.3 $\mu m$ at a pixel size of 4.603 Å) at the ROI. Scale bar, 10 $\mu m$. The same internalized fluorescent beads as in **c** (pink circles) are noted. **f.** Tomographic slice, ~45 nm thick (binned 2x tomogram at a pixel size of 9.206 Å), through the 3X3 montaged cellular tomogram (cyan ROI in **e**). Nucleus, nuclear pore complex (NPC), mitochondria, Golgi apparatus, rough ER, multivesicular bodies (MVB) are noted. Scale bar 1 $\mu m$. The same internalized fluorescent bead (pink circled) as in **c**, **e**, **f** was noted by the asterisk (white).

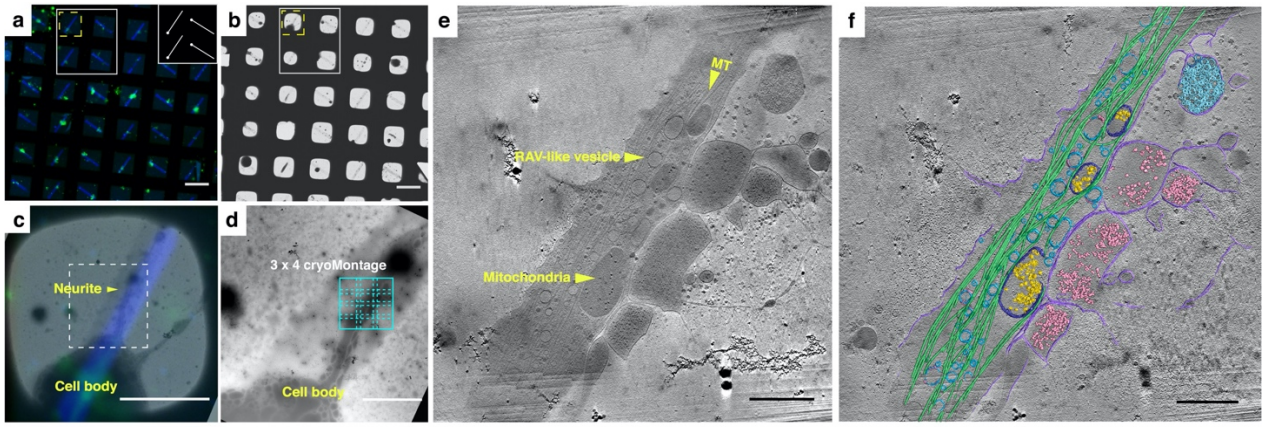


**Fig. 2. Correlative live-cell-FLM and montage cryo-ET of primary *Drosophila melanogaster* neurons on a mask-free micropatterned cryo-TEM grid. a-b.** Live-cell FLM (**a**) and cryo-EM (**b**) grid maps of membrane GFP-labeled primary neurons (green) cultured on a gold-mesh, holey (R1.2/20) carbon film micropatterned with a straight-line pattern (inset in **a**) across the grid and coated with fluorescent concanavalin A (blue) to control the growth of neurites. Scale bars, 100 $\mu m$. **c.** Overlay of correlated FLM-cryo-EM image of the square highlighted in yellow in **a** and **b**. **d.** Enlarged cryo-EM image of the dashed white boxed region in **c**. A 3X3 tiling for montage cryo-ET (cyan, 6.8 x 5.3 $\mu m$ at a pixel size of 4.603 Å) on the region of interest (ROI) extending from the cell body. Scale bars, 50 $\mu m$ in **c**, 10 $\mu m$ in **d**. **e-f.** Tomographic slice of ~45 nm thick (binned 2x tomogram at pixel size of 9.206 Å), reconstructed from the 3X3 montage tilt series at the ROI (**e**) and the corresponding segmentation (**f**). The structured organization of microtubules (MT, green) and the arrangement of surrounding cellular organelles, including mitochondria (dark blue with calcium granules (yellow)), ribosomes (light pink) and ribosome-associated-like vesicles (darker cyan) are noted. Scale bars, 1 $\mu m$.

## Supplementary Figures and Legends

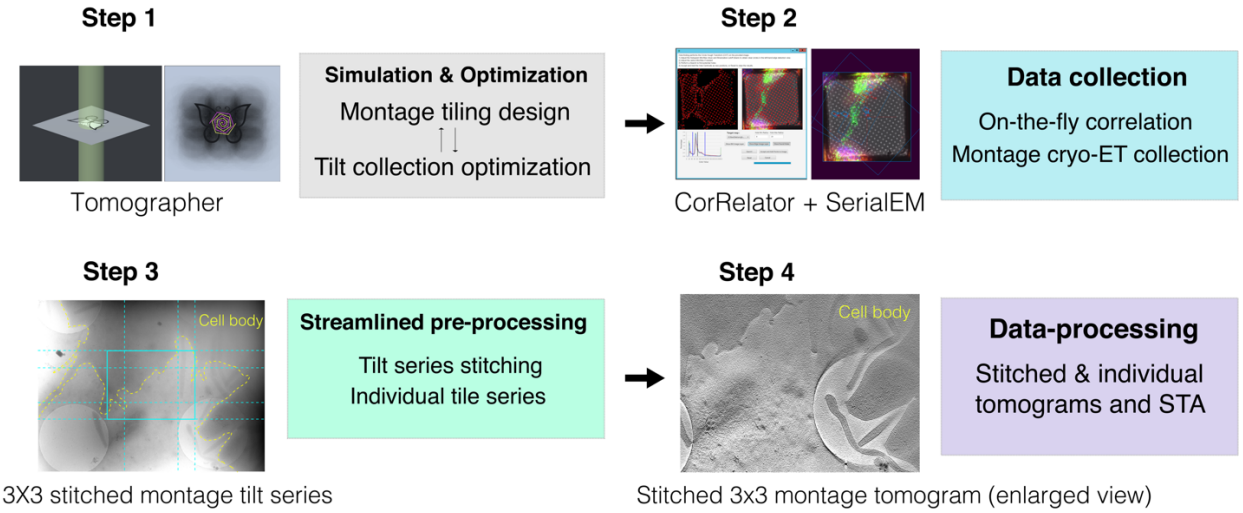


**Supplementary Figure 1. Correlative montage cryo-electron tomography workflow.** The correlative montage cryo-electron tomography (cryo-ET) workflow follows four main steps: **Step 1.** *TomoGrapher* simulation-guided tiling design and optimization of tiling patterns for cryo-ET data collection. **Step 2.** CorRelator-driven 2D and 3D cryo-correlation for high-accuracy targeting to support cryogenic tilt series collection with SerialEM. **Step 3.** Automated pre-processing to sort individual tiles and sub-tilt series, and stitch full montages concurrently with data collection. **Step 4.** Analyses including sub-tomogram averaging (STA) and segmentation may be conducted on both individual and stitched montage tomograms.

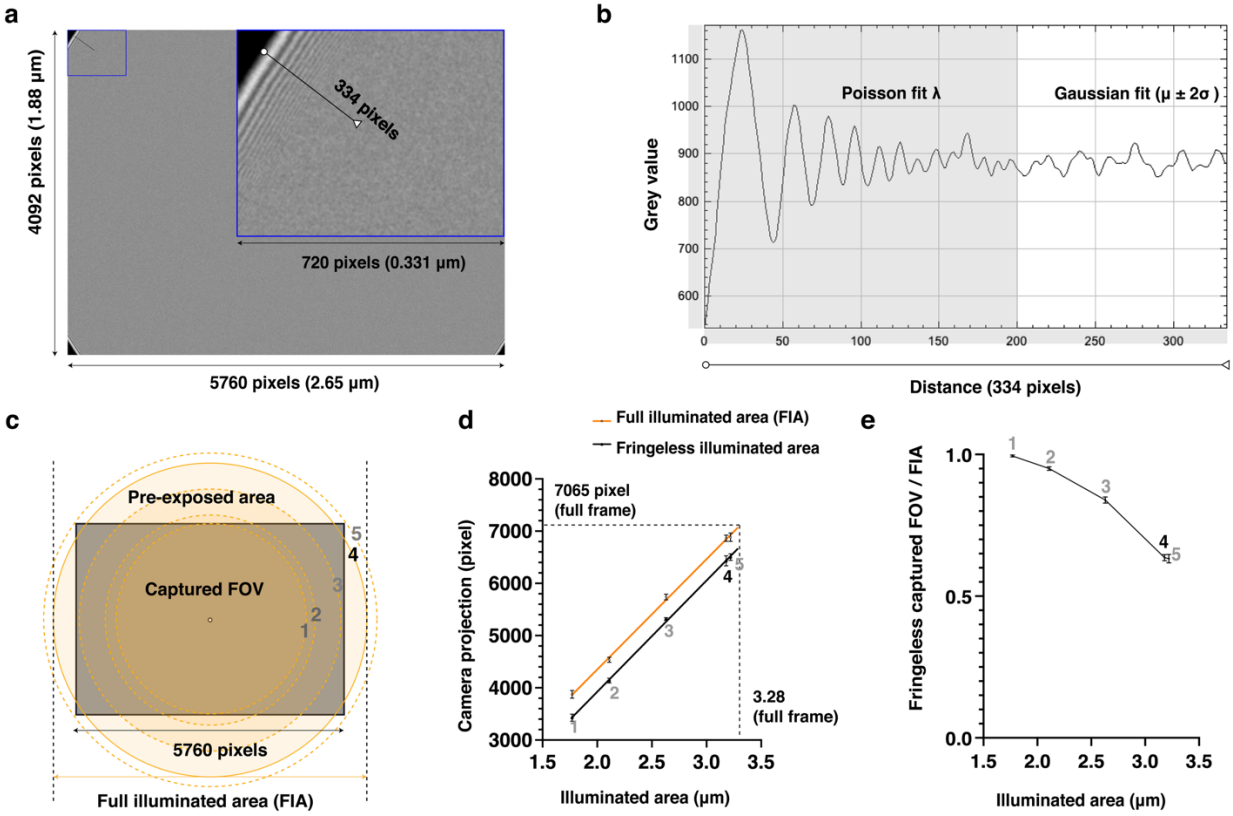


**Supplementary Figure 2. Optimization of beam size and tiling strategy on a triple-condenser lens transmission electron microscope.** Benchmarking of the montage cryo-ET workflow was done on a standard Titan Krios 300 kV microscope system with a K3 camera (5760 X 4092 pixels) at a pixel size of 4.603 Å, C2 aperture of 100 mm, and defocus of -5 $\mu m$. **a.** Fresnel fringes extending over the illuminated area (beam size 3.11 $\mu m$). ***Inset:*** Enlargement of the boxed fringe-containing area, low pass filtered to 50 Å. **b.** Radial intensity profile along the black line in the ***Inset*** of **(a)**. The region visibly impacted by the Fresnel fringes was determined to extend from the beam edge to ~200 pixels (grey area) towards the center of the image, affecting between 3.5 to 4 % of the outer edge of a tile. Based on the Fresnel fringes' Poisson behavior and TEM signal's gaussian distribution, the fringe peak intensities were fit to a Poisson curve (maximum likelihood estimate/peak $\lambda$), considered as "signal" and the fringeless illuminated area was fit to a gaussian function ( $\mu \pm 2\sigma$) as "noise" in MatLab (*poissfit* and *gaussianFit* Curve Fitting Toolbox). The cut-off from "signal" to "noise" were determined as the possibility of "signal" peaks fading into $\mu \pm 2\sigma$ of "noise" distribution, from multiple measurements (n $\geq 3$) along the circular beam edge. **c-e.** Optimization of beam size (1 to 5, beam sizes increase) in consideration of the full illuminated area (FIA), fringeless illuminated area, pre-exposed area, and captured field of view (FOV) at the constant benchmark magnification and defocus. **c.** The camera FOV (rectangle) and projected beam size (circles) extending outside viewable area. **d.** Linear relationships between illuminated areas on a triple-condenser lens Titan Krios system, defined as the electron beam projected onto the sample, and the beam projected size on the camera plane (orange line, orange circles in **c**, *r2* = 0.9989), and the associated fringeless illuminated area (black line, *r2* = 0.9995). **e.** The ratio of fringeless FOV captured on the camera over the full illuminated area (FIA). Overall, beam size 4 (3.11 $\mu m$) achieved reasonable fringeless illumination without wasting electron dose on unimaged yet illuminated sample area, and used for benchmark montage cryo-ET in the paper.

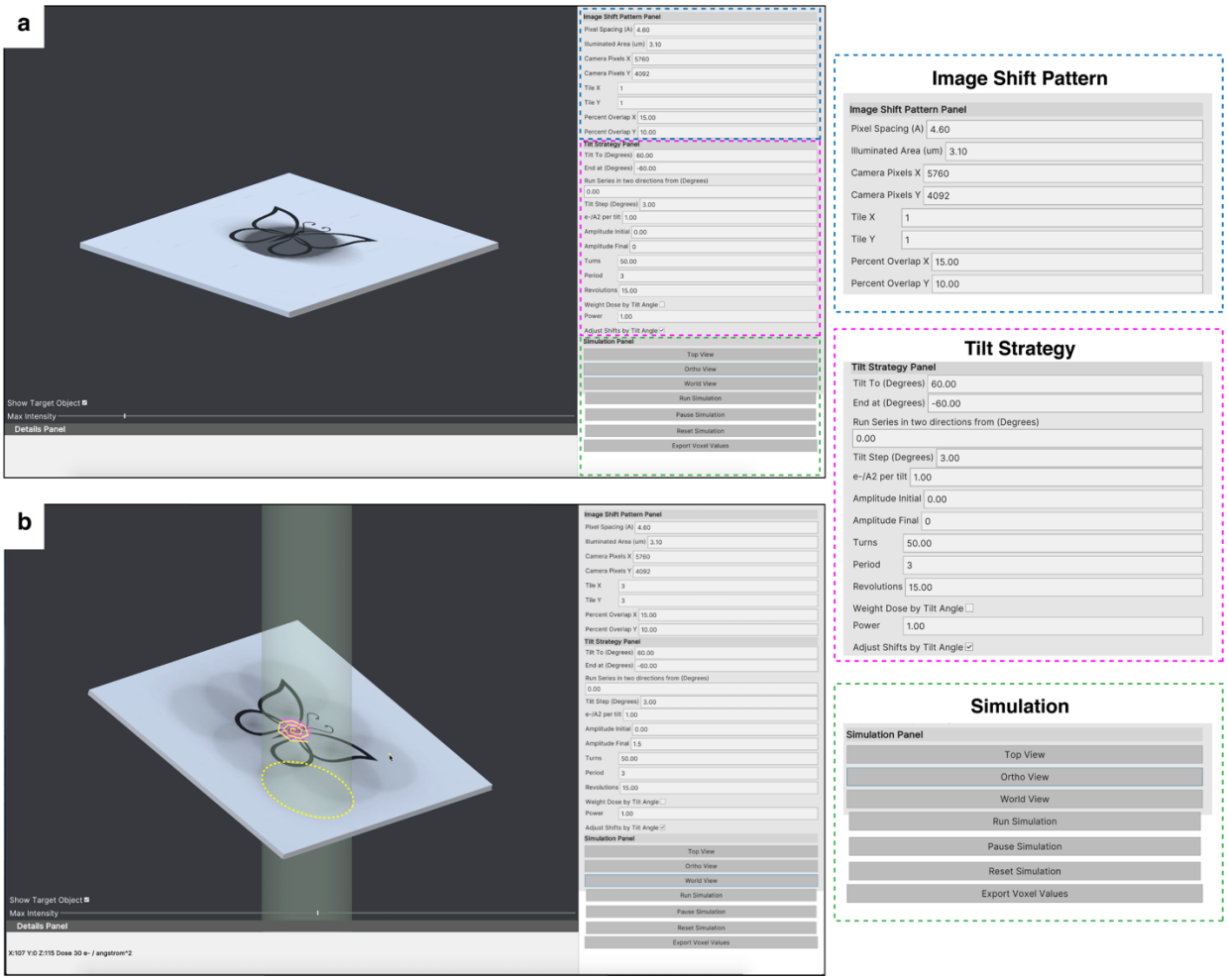


**Supplementary Figure 3. Simulation of tilt series collection in TomoGrapher GUI.** *TomoGrapher* is a simulation tool providing a full 3D visualization of **(a)** single-shot and **(b)** montaged (e.g., 3X3 tile) tilt series collection. A stage comprised of 150 x 150 x 1 voxels with a target region of interest (ROI, butterfly, butterfly, 5 $\mu m$ x 4 $\mu m$ x 0.2 $\mu m$) shows the beam position and accumulated dose values at each position of the total exposed area. The "Image Shift Pattern Panel" (blue boxed) provides parameters to adjust the pixel size, illuminated area (beam size), camera dimensions, and number of and percent overlap for the montage tiles. The "Tilt Strategy Panel" (magenta boxed) controls the tilt range, directionality, tilt step increment, dose per tilt, the amplitudes and geometries of the spiral translational shifts during a tilt series, and provides updated preview images of simulation parameters. Varying intensity as 1/cosine of tilt angle to a certain power is a selectable option to *Weight Dose by Tilt Angle*. Scaling the X-axis shift offset by the cosine of the tilt angle can also be enabled with *Adjust Shifts by Tilt Angle* where the Y-axis is aligned as the tilt axis. The "Simulation Panel" (green boxed) has buttons to change the viewing angle, start a simulation, and export data.

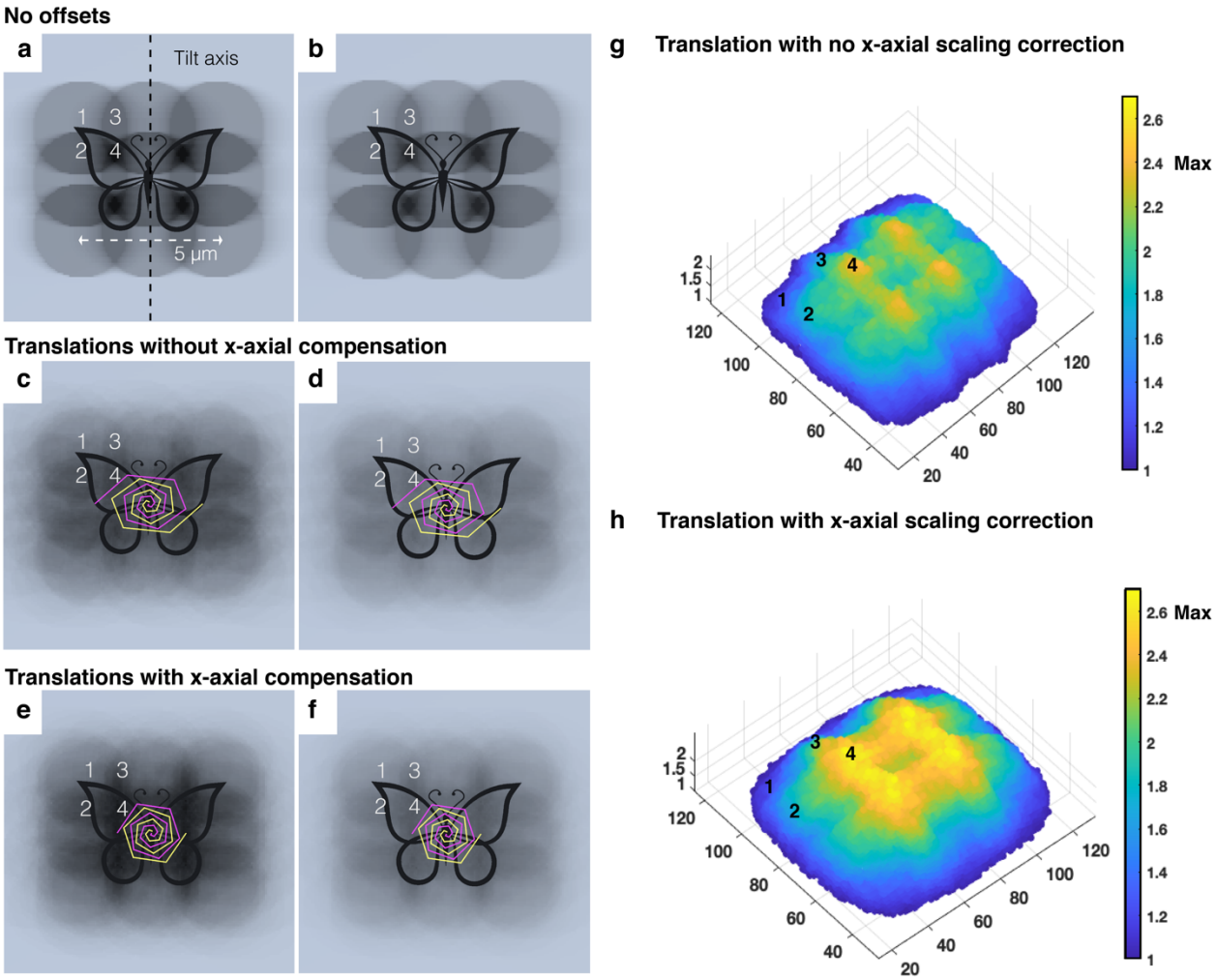


**Supplementary Figure 4. Optimization of montage tiling translational shift for dose distribution in TomoGrapher.** Simulated spatial distribution of dose accumulation in six montage tilt series collection schemes (3X3 tile pattern, pixel size of 4.603 Å, beam size of 3.1 $\mu m$, from -51° to 51° tilts with a 3° increment, the butterfly as ROI), with no translational offsets **(a, b)**, spiral translational offsets **(c, d)**, and the spiral translational shift with an optional scaling factor (cosine of tilt angle) to reduce $x$-axis shifts at higher tilt angles **(e, f)**. Values provided for dose are 1 $e^-/Å^2$ per tile per tilt in **(a, c, d)** and 0.7 $e^-/Å^2$ per tile per tilt in **(b, d, f)**. The accumulated dose at four areas (10 voxels pivoting around the central 1 to 4 points) were compared between the six collection schemes, detailed in **Supplementary Table 1**. The spiral shift pattern is delineated in pink (0° to 51°) and yellow (-51° to 0°) in **(c-f)** where the same global translational offset is applied ($A_{final}$ = 2.5, Period = 3, Turns = 50, Revolutions = 15). **g-h.** Visualization of the dose distribution received by voxels of the ROI butterfly during the tilt series schemes applied in the benchmarking experiments ($A_{final}$ = 1.5, Period = 3, Turns = 50, Revolutions = 15). The simulated dose values ($e/Å^2$/voxel) were exported and plotted in MatLab to show the normalized distribution against the average dose of corresponding tiles from the no translational shift scheme. The same 1-4 center points are marked. The maximum (Max) normalized change is ~2.4-fold in **(g)** and ~2.6-fold in **(h)** with the axial scaling compensation. Height and color of each voxel correspond to its accumulated dose. No axial scaling compensation introduces larger shifts and more dose distribution due to the elliptical projection, but the scaling compensation distributes the dose more evenly.

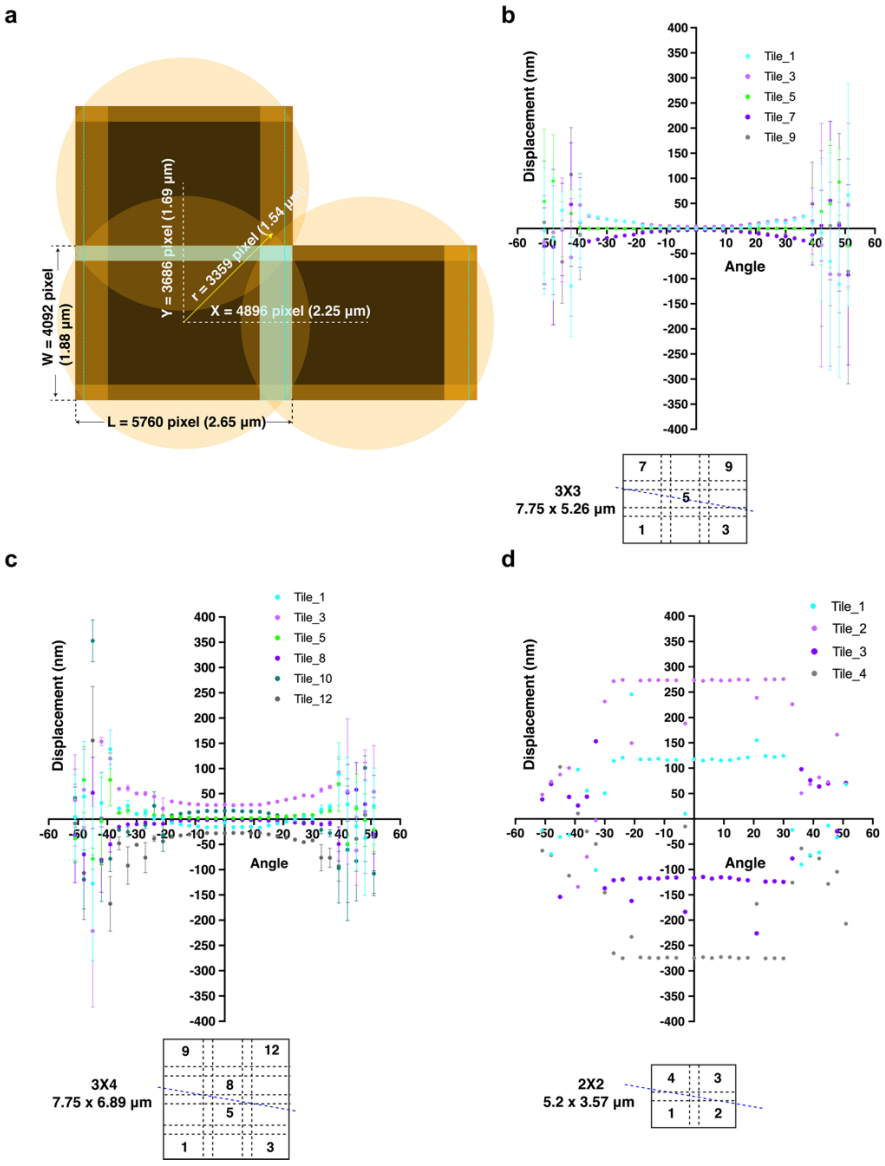


**Supplementary Figure 5. Optimization of the tiling montage cryo-ET tilt series collection with global shift offsets to distribute the electron dose. a.** Strategy for placement of beam tiles (fringeless usable camera FOV / FIA = 0.7) with 15% to 20% in X (Fresnel fringe-affected) and 10% in Y in a square or rectangular array after balancing fringes, pre-exposed area and the ratio of fringeless captured FOV over FIA. Higher overlap in X supports gap-free stitching under low-dose conditions. **b-d.** Shift displacement of individual tiles (blue dotted line notes the tilt axis) of tilt series collected using the benchmark imaging condition on a Titan Krios 300kV (pixel size of 4.603 Å, C2 aperture of 100 mm, defocus of -5 $\mu m$, tilt range of -51° to 51°, 3° increment, dose symmetric scheme with group of 3 tilt angles per switch) with application of an additional translation-only (3X3 in **b** and 3X4 in **c**, maximum global translational offsets of 0.8 $\mu m$, n = 8) or translation plus an additional 20° per tilt rotation offset (total rotation of 35 tilts x 20° = 700°) in (**d**, n = 1) for dose distribution. **d.** Representative plot of tile displacement for a montage tilt series including both translational and rotational shifts which introduce much larger displacements that reduce the effectiveness of automated montage stitching routines. The benchmark spiral

826 parameters ($A_{final}$ = 1.5, Period = 3, Turns = 50, Revolutions = 15) resulted in a ~0.8 $\mu m$ maximum
827 translational offset.

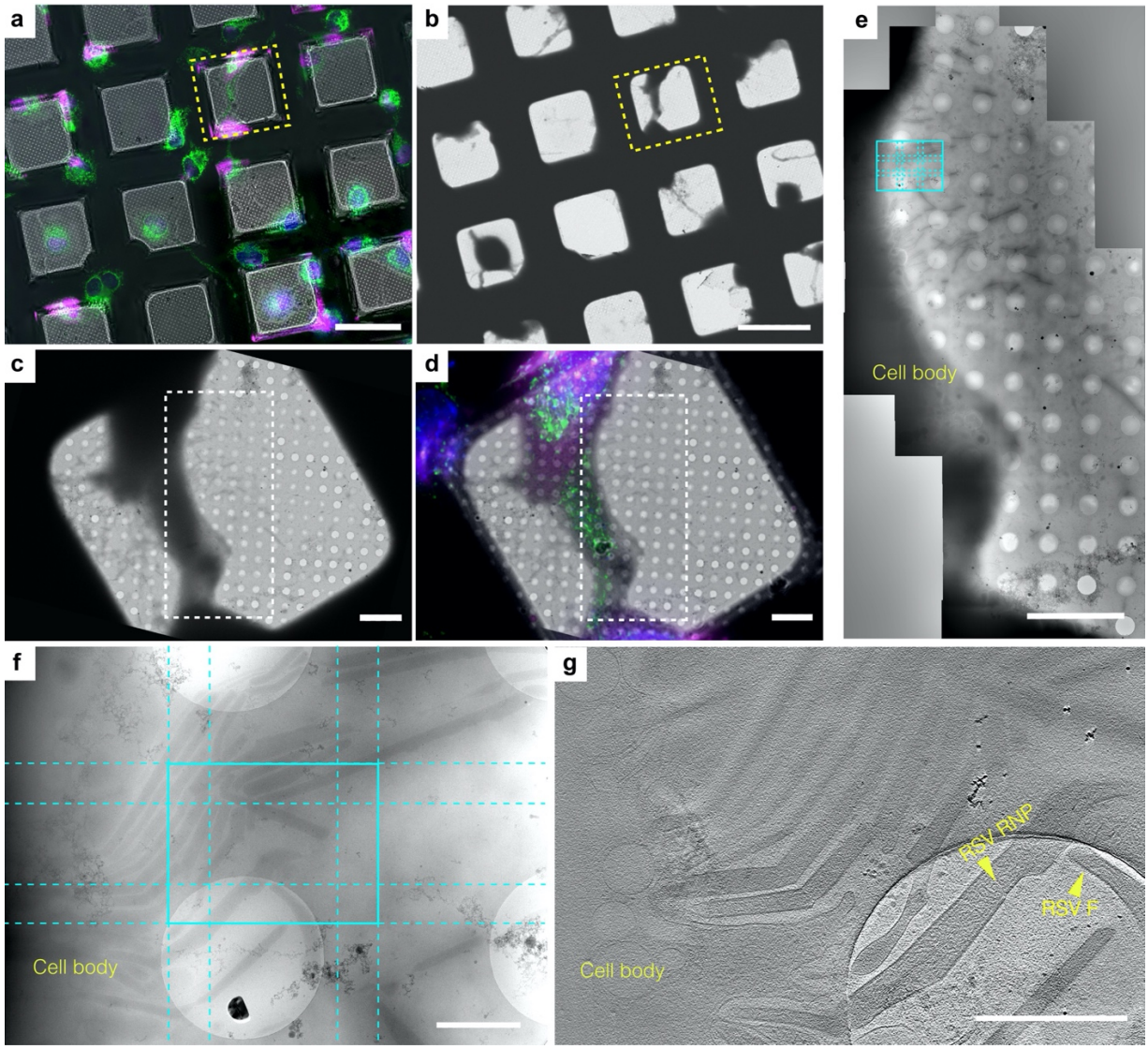


**Supplementary Figure 6. Large field of view of budding RSV virions captured by a correlative cryo-FLM montage cryo-ET workflow.** Cryo-FLM **(a)** and cryo-EM **(b)** grid image montages of RSV-infected HeLa cells (magenta) grown on a $SiO_2$ filmed R2/2 gold-mesh grid. Mitochondria (green) and nucleus (blue) are labeled. Square of interest highlighted in yellow. Scale bars, 100 $\mu m$. **c.** Magnified cryo-EM view of the yellow square in **(b)**. **d.** On-the-fly CorRelator-based cryo-FLM and cryo-EM 2D correlation (yellow square in **a**, **b**) for the ROI identification where montage tilt series were collected in SerialEM. Scale bars, 10 $\mu m$. **e.** Magnified cryo-EM image montage of the white boxed area in **(d)**. A 3X3 tiling for montage cryo-ET at the ROI (cyan tile pattern) where mitochondrion accumulate and RSV actively bud from the cell plasma membrane. Scale bars, 10 $\mu m$. **f.** Montage cryo-ET tiles at 0° tilt (cyan, 6.8 x 5.3 $\mu m$ at pixel size of 4.603 Å). Scale bar, 1 $\mu m$. **g.** Tomographic slice, ~20 nm thick, through the 3X3 montaged tomogram (cyan ROI in **e**, **f**). RSV particles with clearly resolved fusion F glycoproteins and ribonucleoprotein (RNP) complexes are present at budding sites along the cell body. Scale bar, 1 $\mu m$.

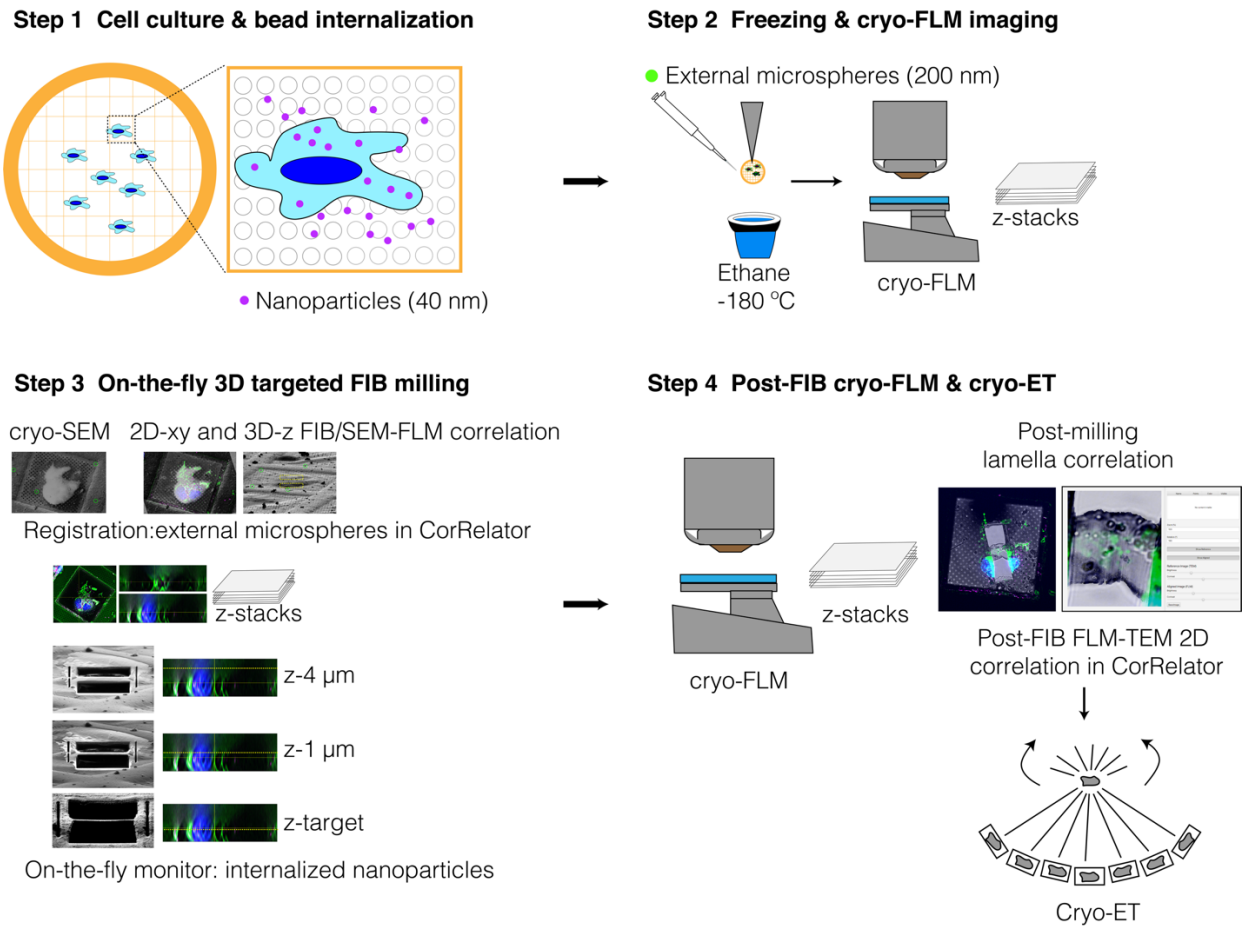


**Supplementary Figure 7. Correlative 3D cryo-FLM-FIB-ET workflow.** Overview of the correlative 3D cryo-FLM-FIB-ET workflow using two fiducial markers: 200 nm external fluorescent microspheres for coarse alignment and registration and cell-internalized 40 nm nanoparticles for on-the-fly 3D correlation during cryo-FIB milling. **Step 1.** Fluorescent nanoparticles (40 nm, pink) incubated with cultured cells were internalized. **Step 2.** Fluorescent microspheres (200 nm) were added prior to plunge freezing and grids were then imaged under a cryo-FLM system to acquire Z-stacks of regions of interest (ROIs). **Step 3.** The same grid was loaded onto and imaged with a dual-beam cryo-FIB-SEM system. Using the 3DCT Toolkit and CorRelator, cryo-FLM Z-stacks and 2D cryo-SEM and cryo-FIB images of ROIs were correlated for milling using 200-nm microspheres (FIB view, green circles) in X, Y, and Z. The placement of the milling boxes was refined based on the relative positions of the nanoparticles (pink) and signal of interest (green). **Step 4.** The same FIB-milled lamella was returned to the cryo-FLM system to acquire a new Z-stack cryo-FLM images for post-FIB-milling correlation. The lamella was then loaded into a cryo-TEM system. CorRelator-directed correlation between cryo-FLM and TEM images of the lamella was performed, and montage or regular tilt series were collected with SerialEM.

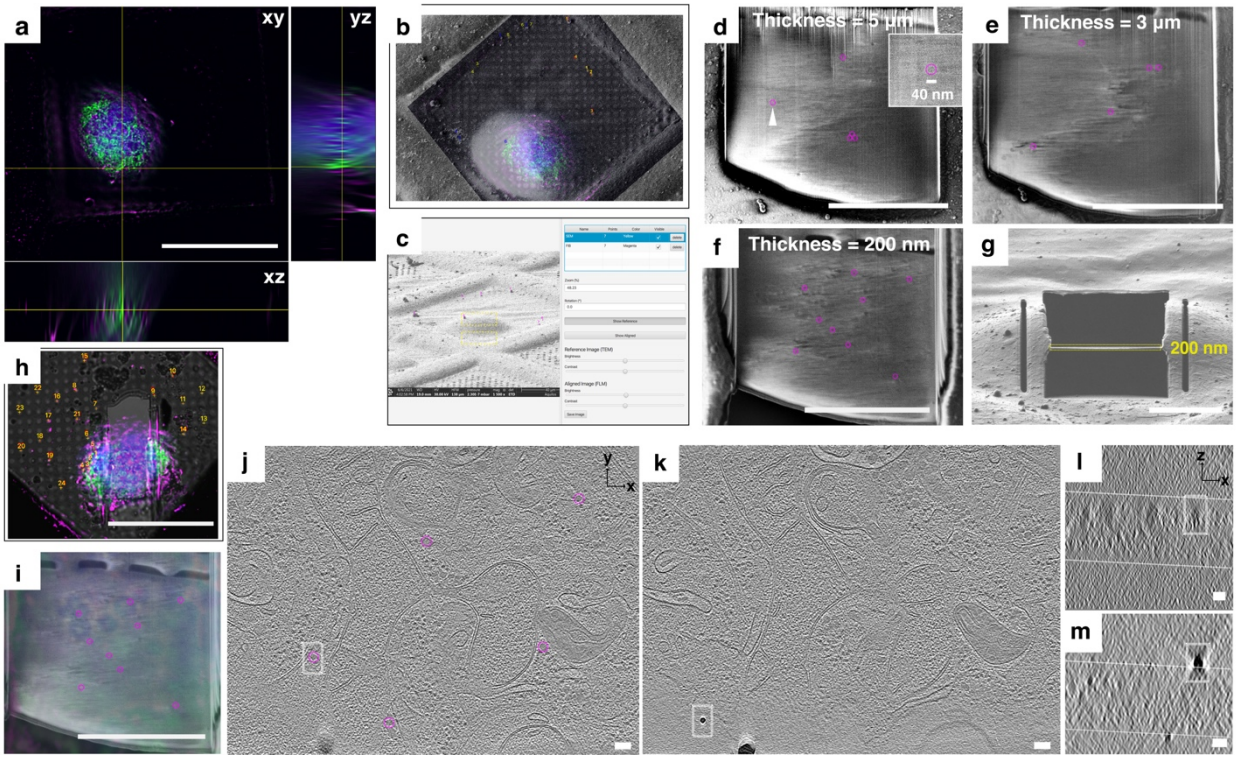


**Supplementary Figure 8. 3D correlation using internalized low-toxic fluorescent beads as fiducial markers in cryo-FIB-SEM. a.** Orthogonal merged deconvoluted fluorescent cryo-FLM (NA = 0.96) projections of labeled mitochondria (green), nucleus (blue), and internalized nanoparticle (pink) inside the HeLa cell. Scale bar, 100 $\mu m$. **b-h.** On-the-fly 3D targeted FIB-milling delineated in the Step 3 in Supplementary Figure 6. The X-Y plane correlation is done in CorRelator **(b)** and initial X-Z correlation to position milling boxes in Z (yellow boxes) done in 3DCT and CorRelator **(c)**. Nanoparticle intensity visible under cryo-SEM as the lamella milling progresses from a thickness of 5 $\mu m$ **(d)** to 3 $\mu m$ **(e)**, to the final 200 nm **(f, g)**, highlighted by pink circles (40 nm in diameter). A representative nanoparticle in **(d)** was pointed out by white triangle and enlarged in the inset. **h-i.** 3D cryo-FLM post-correlation of the post-FIB lamella and pre-FIB corresponding fluorescent section in CorRelator. The corresponding nanoparticles in **(f)** are highlighted in pink circles. Scale bars, 10 $\mu m$ in **(d-g)** and **(i)**, 50 $\mu m$ in **(h)**. Red and yellow numbers in the GUI screenshots of **(b, c, h)** are registration points used in CorRelator. **j-m.** Representative X-Y tomographic slices (thickness of 20 nm, pixel size of 4.603 Å) displaying the nanoparticles (pink circle, **j**) and similar sized non-nanoparticle intensity (white boxed, **k**), and their corresponding X-Z projections **(l-m)** of white boxed area in **(j)** and **(k)**. The tomogram Z-volume boundaries are indicated by white dashed lines in **(l-m)**. Scale bars, 50 nm in **(j-m)**. Nanoparticles are less electron dense than ice particles or regular gold fiducials.

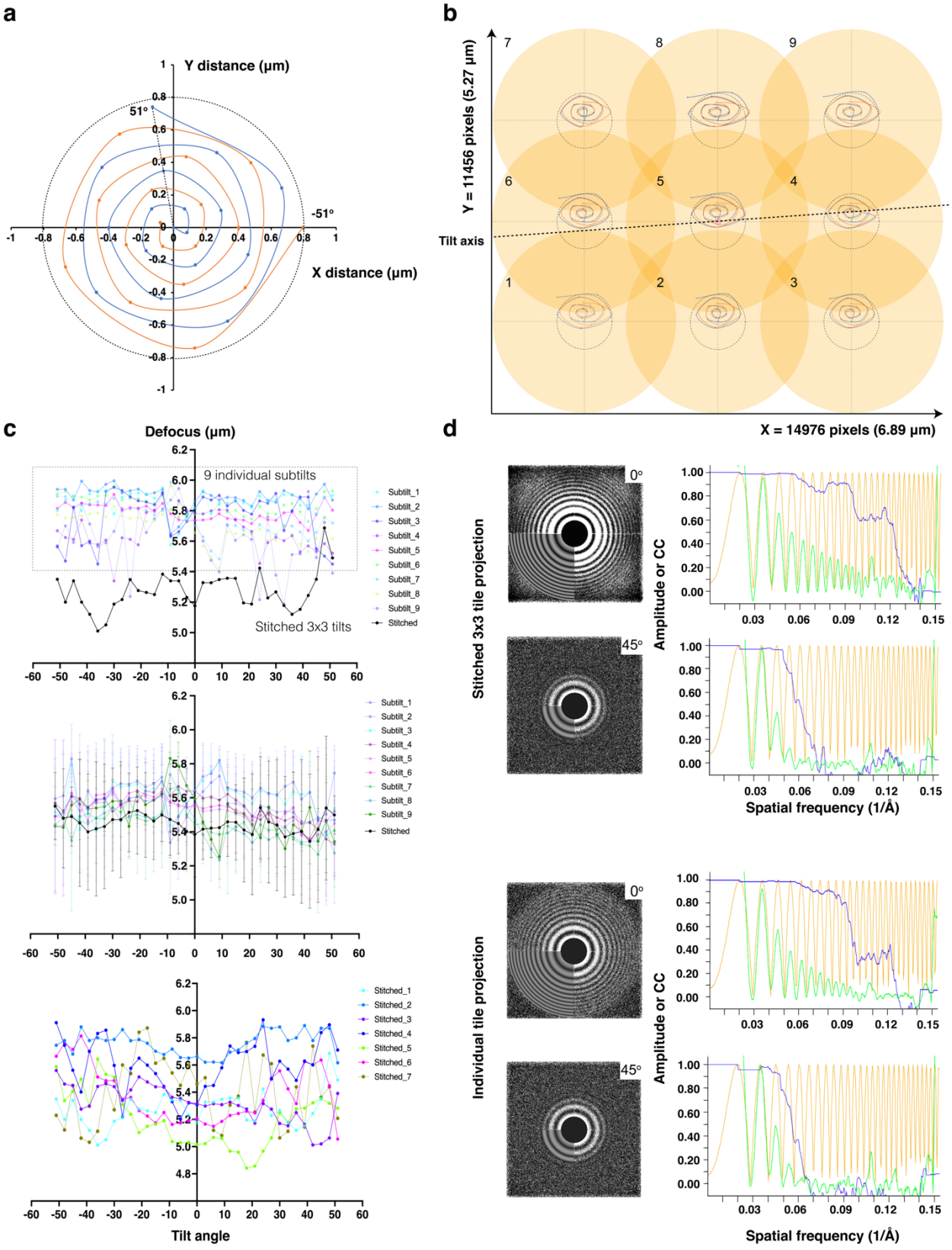

**Supplementary Figure 9. Defocus determination and CTF estimation of full stitched montage and individual tile tilt series. a.** Benchmark spiral translation pattern applied to distribute electron dose. To introduce global translation offsets, the central tile of the montage follows spiral paths shifting outwards over the full course of the tilt series from -51° (orange points) to 51° (blue points) in a dose-symmetric, three-degree increment and group of 3 scheme. The translation maximum is 0.8 $\mu m$ (black dotted circle, $A_{final}$ = 1.5, Period = 3, Revolution = 15 as spiral shape parameters). **b.** Cross-correlation alignment of cosine-stretched image shifts at each tilt angle relative to 0° tilt in individual tile tilt series of the regular 3X3 montage pattern, using Tiltxcorr in IMOD. The image shift between each tilt follows a stretched spiral along the X axis when the optional scaling parameter of the translation is not applied. The image shifts of individual tile tilt series were overall within the maximum distance of 0.8 $\mu m$ (black dotted circle). Numbers indicate the individual tile positions applied to both **(c)** and **(d)**. **c.** Defocus values of nine individual tile sub-tilt series and the corresponding stitched 3X3 montage tilt series (pixel size of 4.603 Å), following the same global spiral shift in **(a, b)** were estimated using CTFPLOTTER in IMOD: one representative 3X3 stitched montage and nine individual tile tilt series (top), median variation at each tilt angle over multiple 3X3 montage and corresponding tile tilt series (n = 3, middle), and 7 stitched montage tilt series (bottom) are shown. A target defocus of -5 $\mu m$ was applied by performing autofocusing prior to the tile collection at each tilt angle, along the tilt axis, 7.5 $\mu m$ away from the center of the montage tile to account for the size of the montage (6.89 x 5.27 $\mu m$) and additional translation shift (0.8 $\mu m$). **d.** CTF estimation in CTFFIND4 by the 2D power spectra (left) from projections at 0°, 45°, and -45° from a representative 3X3 stitched montage tilt series and one of the individual tile tilt series (tile position 2 in **b**), and corresponding fitted 1D models (right) showing radially averaged amplitude spectrum (green), CTF fit (orange), and CTF fit score (blue).

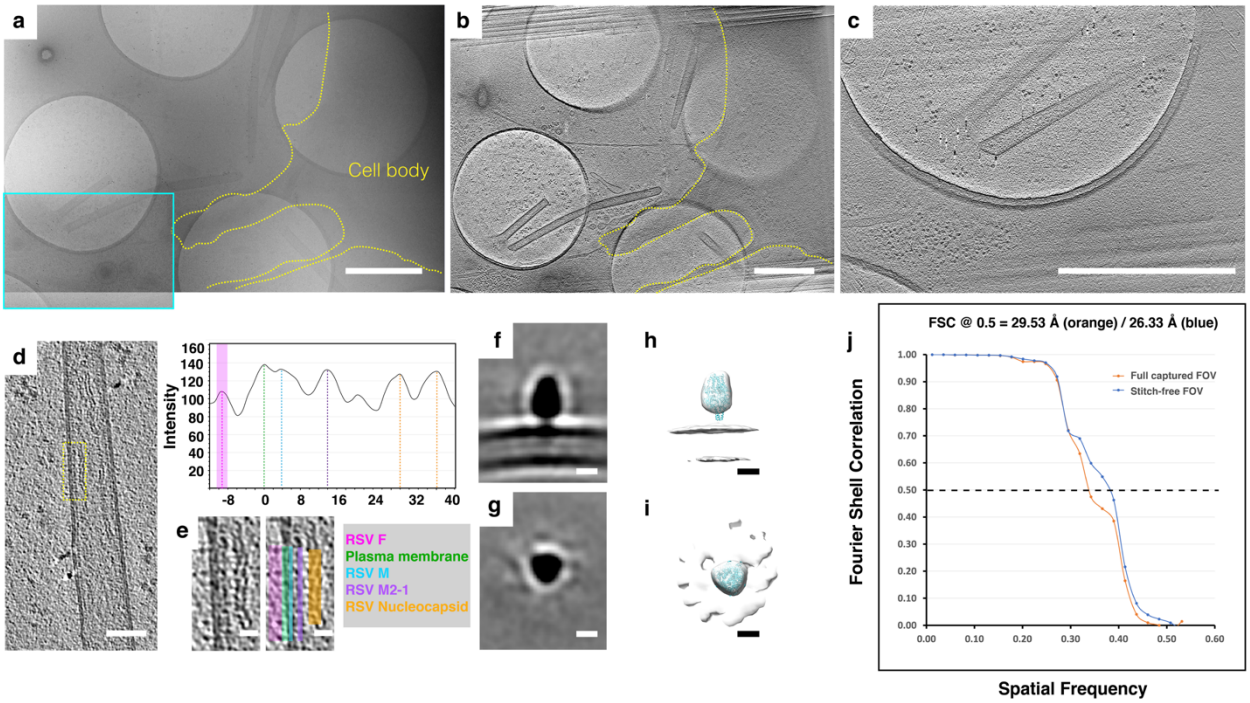


**Supplementary Figure 10. Sub-tomogram averaging of individual tile tomograms. a.** 3X3 montage cryo-ET image tiles at 0° tilt of RSV-infected BEAS-2B cells. The cell boundary is delineated in yellow and one tile with viruses used for sub-tomogram averaging is highlighted in cyan. **b.** Central slice of the stitched 3X3 montage tomogram in **(a)**, cell boundary (yellow). **c.** Central ~18 nm slice of the reconstructed tomogram (pixel size of 9.206 Å) of the tile highlighted in (**a**, cyan box). Scale bars, 1 $\mu m$ in **a-c**. **d.** Reoriented Z-projection (9 nm thick) of the virion from the tomogram in **(c)**. **e.** An enlarged view of virus (yellow dashed box in **d**) with virion components noted in different colors and a linear density profile across the virion region. Scale bars, 100 nm in **(d)**, 20 nm in **(e)**. **f-i.** Sub-tomogram averages of RSV F from individual tile tomograms collected through the 3X3 montage cryo-ET workflow. The particles in overlapped stitched zones (15% in X and 10% in Y) were excluded. **f-g.** Slices from a sub-tomogram average of binned 2 individual tile tomograms (pixel size of 9.206 Å) of RSV F filtered to 27 Å in the side (**f**) and top (**g**) views. **h-i.** RSV pre-fusion trimer model (PDB: 4JHW, cyan) fit into an isosurface of the sub-tomogram average of F. Scale bars, 5 nm. **j.** FSC curves for sub-tomogram averages of F particles picked from full captured field of view (orange, C3 symmetry expansion, n = 23250) and field of view free from stitching overlaps (blue, C3 symmetry expansion, n = 20707) as stitch-free particles in sub-tilt tomograms.

954

| | Position 1 (x/y, 38/101) | Position 2 (x/y, 45/87) | Position 3 (x/y, 59/103) | Position 4 (x/y, 58/87) |
|---|---|---|---|---|
| **No translation (a)** | 39.2 $\pm$ 5.2 | 85.1 $\pm$ 18.1 | 64.5 $\pm$ 7.7 | 105.1 $\pm$ 18.5 |
| **No translation lower dose by 30% (b)** | 27.5 $\pm$ 3.6 | 59.6 $\pm$ 12.5 | 45.2 $\pm$ 5.3 | 73.6 $\pm$ 12.9 |
| **Translation (c)** | 45.5 $\pm$ 3.2 | 77.1 $\pm$ 4.8 | 56.8 $\pm$ 7.4 | 79.2 $\pm$ 10.1 |
| **Translation lower dose by 30% (d)** | 31.8 $\pm$ 2.2 | 48.2 $\pm$ 3.3 | 39.8 $\pm$ 5.2 | 56.1 $\pm$ 7.1 |
| **Translation with x-axial correction (e)** | 45.2 $\pm$ 4.8 | 83.7 $\pm$ 10.8 | 66.7 $\pm$ 7.6 | 94.7 $\pm$ 10.8 |
| **Translation with x-axial correction lower dose by 30% (f)** | 31.7 $\pm$ 3.4 | 51.2 $\pm$ 7.6 | 46. 7 $\pm$ 5.3 | 66.3 $\pm$ 7.5 |

955

956 **Supplementary Table 1**. Dose accumulation in $e^-/Å^2$/voxel at specified voxels in four sampling
957 areas (radius of 10 x 10 x 1 voxel$^2$ pivoting around the central sampling points 1 to 4, X and Y
958 voxel positions specified, indicated in **Supplementary Fig. 4**) of six different collection schemes
959 with the same 3X3 montage tile pattern using *TomoGrapher* simulation. The mean and standard
960 deviation were calculated. The Tilt Strategy parameters is also specified in Supplementary Fig. 4
961 (3X3 tile pattern, pixel size of 4.603 Å, beam size of 3.1 $\mu m$, from -51° to 51° tilts with a 3°
962 increment, 1 or 0.7 $e^-/Å^2$ per tile per tilt).
963